

Investigation and Comparison of Different Numerical In- and Outflow Boundary Conditions for Simulation of Turbomachinery Flows

Master Thesis

Daniel Zilles

Rheinisch-Westfälische Technische Hochschule Aachen
Aerodynamisches Institut
Wüllnerstr. 5a
52062 Aachen

Examiner: Univ.-Prof. Dr.-Ing. W. Schröder
Supervising Assistant: M.Sc. T. Hösgen
July 2020

Contents

List of Figures	IV
Nomenclature	XI
1 Introduction	1
1.1 Motivation	1
1.2 Current State of Research	2
2 Mathematical Model	4
2.1 Governing Equations	4
2.2 Numerical Method	5
3 Characteristic Boundary Equations	8
3.1 Derivation of the Characteristic Form of the Navier-Stokes Equations	8
3.2 Derivation of the LODI and the 3D-NSCBC System	10
3.3 Different Formulations of the 3D-NSCBC System	13
3.4 Derivation of the Wave Amplitude Variations for Different Boundary Conditions	16
3.5 Implementation	22
3.6 Injection of Turbulence	22
4 Validation of the Implemented Characteristic Boundary Conditions	24
4.1 Convergence in a Flow Channel with Periodic Boundaries	24
4.2 Turbulence Injection into a Flow Channel	27
4.3 Ability of the Outflow CBC to Represent a Rotational Flow	30
4.4 Permeability of the Characteristic Outflow Boundary Condition for a Vortex	32
4.5 Reflectivity of the Characteristic Inflow and Outflow Boundary Conditions for Acoustic Waves	35

5	Application in a Turbine-Like Setup	39
5.1	Main Flow	43
5.2	Turbulence Injection into the Main Flow	45
5.3	Wheel Space Flow	46
5.4	Evaluation of the Spectral Sound Pressure Level	53
6	Conclusion	55

List of Figures

3.1	Characteristic waves leaving and entering the computational domain [16]. . . .	11
4.1	Slice of the computational domain of the flow channel at $x_2 = 0$	25
4.2	Convergence of the Mach number and the at the CBC imposed values. . . .	26
4.3	Reynolds stresses $\langle \langle \rho u'_i u'_i \rangle_t \rangle_{x_2 x_3}$ spatially averaged over the x_2 - x_3 -planes, temporally averaged and normalized with the injected mean Reynolds stresses $(\rho u'_i u'_i)_{in}$	29
4.4	Turbulent kinetic energy $\langle \langle TKE \rangle_t \rangle_{x_2 x_3}$ spatially averaged over the x_2 - x_3 -planes, temporally averaged and normalized with the injected mean turbulent kinetic energy $(TKE)_{in}$	29
4.5	Slice of the computational domain of the annulus geometry at $x_1 = 0$	31
4.6	Pressure equilibrium at the outflow boundary for different relaxation coefficients σ^* compared to the analytical solution.	32
4.7	Vortex leaving the computational domain through the Neumann and Dirichlet type boundary condition in Eq. (2.14). Slice at $x_3 = 0$	33
4.8	Vortex leaving the computational domain through the CBC in Eq. (3.53). Relaxation coefficient $\sigma^* = 0.25$. Slice at $x_3 = 0$	34
4.9	Pressure and total velocity fluctuations at the line $x_2 = 0$ and $x_3 = 0$. Time $t = 74.7$	35
4.10	Test case E3: $\eta_k = 0.02$, $\sigma^* = 0.25$. Injected pressure waves leaving the computational domain. Reflections of those pressure waves can be observed in Fig. 4.10d.	37
4.11	Reflections of the injected acoustic waves at $t = 156.25$ spatially averaged over the x_2 - x_3 -planes.	38
5.1	Computational domain of the turbine-like test case.	42
5.2	Mass flow rate through a plane of the main annulus at $x_1 = -15$	43
5.3	Imposed values at the main annulus inflow and outflow of test case F3. . . .	44

5.4	Reynolds stresses $\langle \langle u'_i u'_i \rangle_t \rangle_{x_2, x_3}$ and the turbulent kinetic energy $\langle \langle TKE \rangle_t \rangle_{x_2, x_3}$ spatially averaged over the x_2 - x_3 -planes of the main annulus, temporally averaged and normalized with the injected mean values $(\rho u'_i u'_i)_{in}$ and $(TKE)_{in}$.	45
5.5	Imposed values at the wheel space inflow of the test case F3.	46
5.6	Mass flow rates through the wheel space.	47
5.7	Instantaneous pressure fields in the wheel space at $t/t_{ref} \approx 71$ and without turbulence injection.	49
5.8	Instantaneous density fields in the wheel space at $x_3 = 69$, $t/t_{ref} \approx 71$ and without turbulence injection.	50
5.9	Time averaged velocity fields $\langle u_2 \rangle_t$ in the wheel space at $x_2 = 0$	51
5.10	Time averaged velocity fields $\langle u_3 \rangle_t$ in the wheel space at $x_2 = 0$	52
5.11	Spectral sound pressure level for various planes of the test cases F1 and F3. .	53

Nomenclature

Acronyms

3D-NSCBC	Three-Dimensional Navier-Stokes Characteristic Boundary Condition
ALE	Arbitrary Lagrangian-Eulerian
BC	Boundary Condition
CBC	Characteristic Boundary Condition
LES	Large-Eddy Simulation
LODI	Local One-Dimensional Inviscid
NSCBC	Navier-Stokes Characteristic Boundary Condition
RANS	Reynolds-Averaged Navier-Stokes
RWTH	Rheinisch-Westfälische Technische Hochschule
URANS	Unsteady Reynolds-Averaged Navier-Stokes
ZFS	Zonal Flow Solver

Dimensionless Numbers

M	Mach number
M_∞	prescribed Mach number
M_{max}	maximum Mach number at the boundary
Pr	Prandtl number
Re	Reynolds number
Sc	Schmidt number
Str	Strouhal number

Superscripts

$'$	fluctuating
$'/'$	corrected
i	interpolated, inertial
k	Runge-Kutta step
mf	main flow
n	time step
$turb$	including turbulent contribution
wsf	wheel space flow

Operator

\cdot	dot product
$\langle \cdot \rangle_{\mathbf{x}}, \langle \cdot \rangle_{x_2, x_3}$	average operator in space
$\langle \cdot \rangle_t$	average operator in time
$\mathbf{R}(t, \mathbf{Q})$	residual operator
∇	nabla operator
∂	partial differential operator
$\zeta(\Phi)$	sign of the velocity term
d	differential operator
$Ei(\cdot)$	exponential integral function
$exp(\cdot)$	exponential operator
$log(\cdot)$	logarithmic operator
$N(\Phi, \Psi)$	normal distribution, Φ : mean value , Ψ : standard deviation

Subscripts

0	stagnation state
Φ	indices of the acoustic characteristic variables

c	cut cell
d	dimensional variable
in	inflow
inv	inviscid
n	normal direction
out	outflow
t	tangential directions
vis	viscid
w	wall

Symbols

β	transverse damping parameter for the outflow CBC
α, α_k	Runge-Kutta coefficients
$\eta, \eta_k, \eta^*, \eta_k^*$	inflow relaxation coefficients
$\mathcal{C}, \mathcal{C}_k$	combined tangential and viscous terms
$\mathcal{D}, \mathcal{D}_k$	viscous terms
$\mathcal{L}, \mathcal{L}_k$	wave amplitude variations
$\mathcal{T}, \mathcal{T}_k$	tangential terms
D	viscous terms in quasi-conservative form
Δt	time step size, time interval
Δx	discretization size
Δx_i	distance interval in i -direction
δ_{ji}	Kronecker's delta
\dot{m}	mass flow rate
η	dynamic viscosity
Γ	computational domain

γ	ratio of specific heats
\mathbf{d}	wave amplitude variations in primitive form
\mathbf{D}_c	mass defect of cut cell
\mathbf{n}	outward unit normal vector
\mathbf{Q}	vector of conservative variables
\mathbf{q}	vector of heat conduction
\mathbf{RHS}, RHS_k	residual in quasi-conservative form
\mathbf{t}_{ik}	eigenvalue vector
\mathbf{u}, u_i	velocity vector, velocity component
\mathbf{V}	vector of primitive variables
\mathbf{x}, x_i	Cartesian coordinates
\mathcal{C}_e	combined tangential and viscous terms of the NSCBC expression of the kinetic energy
\mathcal{C}_M	combined tangential and viscous terms of the NSCBC expression of the square Mach number
\mathcal{C}_{pt}	combined tangential and viscous terms of the NSCBC expression of the total pressure
\mathcal{C}_{Tt}	combined tangential and viscous terms of the NSCBC expression of the total temperature
\mathcal{C}_T	combined tangential and viscous terms of the NSCBC expression of the static temperature
ω	wavelength
ρ	density
σ, σ^*	outflow relaxation coefficient
τ_t	turbulent time scale
$\underline{\mathbf{A}}_i$	quasi-conservative Jacobian matrix of the fluxes
$\underline{\mathbf{H}}$	flux tensor

$\underline{\mathbf{I}}$	unity tensor
$\underline{\mathbf{P}}$	Jacobian matrix
$\underline{\mathbf{T}}_i$	eigenvalue matrix
$\underline{\Lambda}_i, \lambda_{ik}$	eigenvalues
ϵ_{ijk}	permutation tensor
$\underline{\boldsymbol{\tau}}$	deviatoric stress tensor
φ	cylindrical angle
A	surface area
a	speed of sound
a_{ki}	Cholesky decomposition of the Reynolds stress tensor
c_1	free vortex strength
c_2	vortex strength
c_p	specific heat capacity at constant pressure
c_v	specific heat capacity at constant volume
D	diffusion coefficient
E	total specific energy
e	internal specific energy
e_c	kinetic energy
f	frequency
f_s	sampling frequency
h	hamming window size
J_Y	diffusive flux
k	thermal conductivity
L	domain length in x_1 -direction
l	neighbor of cut cell

L_t	turbulent length scale
L_{ref}	reference length
M_c	neighborhood of cut cell
n	normal direction
n_s	number of samples
N_{rm}	number of Fourier modes
ol	overlap
p	static pressure
p_s	spectral pressure fluctuations
p_t	total pressure
p_{ac}	pressure amplitude of acoustic wave
p_{ref}	human hearing threshold
p_{se}	pressure of the simplified equilibrium equations
r	radial coordinate
r_+	outer annulus radius
r_-	inner annulus radius
R_d	specific gas constant
r_v	characteristic vortex radius
S	Sutherland's constant
s	number of Runge-Kutta steps
SPL	sound pressure level
T	static temperature
t	time
T_t	total temperature
t_{ref}	traversal time from inflow to outflow

TKE	turbulent kinetic energy
u_φ	angular velocity
V	control volume
Y	concentration of the passive scalar

Chapter 1

Introduction

1.1 Motivation

In turbomachinery applications, hot gas from the main flow can enter the cavity between the rotor and the stator. Since in modern turbomachinery, main flow temperatures lie above the melting points of the turbine materials, an ingress of hot gas into the rotor-stator wheel space can lead to overheating and damage of the machine. To improve the understanding of the flow inside the wheel space, full 360° Large-Eddy Simulation (LES) of axial flow turbines including the wheel space are conducted at the Institute of Aerodynamics at RWTH Aachen University [15]. As the turbine main flow is highly turbulent, and the flow inside the wheel space is driven by fluctuations generated by the interaction of main flow and wheel space flow, the handling of turbulent fluctuations is very important. Numerical studies showed the advantages of a LES approach compared to Reynolds-Averaged Navier-Stokes (RANS) and Unsteady Reynolds-Averaged Navier-Stokes (URANS) approaches in order to predict the complex flow inside the wheel space and the interactions between wheel space flow and main flow. O'Mahoney et al. [14] conducted a simulation of a turbine segment including blades. They showed that LES gives a higher agreement with experimental data in terms of sealing effectiveness compared to URANS. Gao et al. [6] compared LES, RANS and URANS in a simulation of a turbine segment without blades to experimental data. They showed that LES achieved the best agreement with the measured mean pressure distribution. Regardless both, O'Mahoney et al. and Gao et al., showed discrepancies between the experimental data and the LES and refer to a possible connection to the limited sector angle. It should be noted, that the conduction of full 360° LES of turbomachinery applications is computationally expensive.

Compared to LES, the RANS and URANS approaches are not resolved in time or not resolving all time scales leading to the loss of the ability to represent the unsteady fluctuations. In LES, the large-scale, energy-containing, turbulent fluctuations are resolved. Therefore, im-

posing the inflow and outflow boundary conditions of turbulent flows in LES is numerically challenging. When turbulent eddies cross the outflow boundaries, they can locally switch the behavior from outflow to inflow. Further, when eddies cross the boundaries, fluctuations are generated which are reflected back into the domain and distort the solution. This can increase the simulation's time to convergence. The common approach to circumvent these issues is to use sponge layers at the domain boundaries to damp the turbulent fluctuations and pressure waves approaching the boundaries.

In this thesis, several different numerical approaches for imposing boundary conditions in LES are analyzed and tested for different simplified flow configurations resembling an axial flow turbine. The focus is set on the class of Navier-Stokes Characteristic Boundary Conditions (NSCBC) introduced by Poinot et al. [16] in 1991. The main intention is to investigate possible improvements in the rate of convergence and reduction of the computational cost by applying NSCBC. First, the implementation of the investigated boundary conditions will be validated, and second, the performance will be compared to a set of Neumann and Dirichlet type boundary conditions in means of convergence to a quasi steady flow state.

1.2 Current State of Research

The NSCBC are a group of boundary conditions that use the characteristics of the Navier-Stokes equations to develop a physical formulation of the boundary condition. Because of the consideration of the characteristic waves crossing the boundaries, non-reflecting and partially non-reflecting boundary conditions can be derived.

The Characteristic Boundary Conditions (CBC) for hyperbolic systems were first introduced by Thompson [22]. Later, Poinot et al. [16] applied the approach of Thompson on the Navier-Stokes equations and presented an approach to derive CBC for different sets of primitive variables to be imposed. In this NSCBC approach, Poinot et al. assume that the flow is normal to the boundary, and neglect all characteristic waves tangential to the boundary and the viscous effects. This results in the Local One-Dimensional Inviscid (LODI) formulation which can be used to obtain multiple CBC.

Yoo et al. [25] appended the LODI system with the tangential characteristics, and introduced a damping term for the tangential terms in outflow boundary conditions showing that this leads to a more stable method for flows with significant velocity distributions in the boundary transverse terms. Further, Yoo et al. [24] included viscous terms and source terms for reactive flows into the CBC. Lodato et al. [11] discussed the necessity of a special treatment at edges and corners of the boundary in case the tangential terms are taken into account. They applied the extended LODI equations including tangential terms in three dimensions

to a free jet and an impinging round-jet flow configuration. These extensions to the LODI problem result in the so called Three-Dimensional NSCBC approach (3D-NSCBC).

Flows in turbomachines are challenging. The strategies, addressing these challenges and discussed in this thesis, are summarized in the following. At the outflow boundaries the flow is strongly rotational. This has been addressed by Koupper et al. [9], who showed that the CBC are able to represent a rotating flow at the outflow boundary while imposing a mean static pressure and remaining non-reflective by applying a patch-averaged formalism. Furthermore, to represent the flow in a realistic turbomachine, a synthetic turbulence is commonly imposed at the inflow boundaries. The injection of turbulence was part of the work of Prosser [17] and Guézennec et al. [8], who split the characteristic waves into an inertial and an acoustic part by a low Mach number expansion. This consideration allows to inject turbulence, while maintaining the partially non-reflecting behavior of the boundary condition. Odier et al. [13] derived a set of partially non-reflecting characteristic inflow boundary conditions imposing total quantities and compatible to turbulence injection.

Chapter 2

Mathematical Model

2.1 Governing Equations

The Navier-Stokes equations for a viscous, compressible fluid in non-dimensional, conservative form are given in the Arbitrary Lagrangian-Eulerian (ALE) formulation by

$$\frac{d}{dt} \int_V \mathbf{Q} dV + \oint_{\partial V} \underline{\mathbf{H}} \cdot \mathbf{n} dA = 0 \quad (2.1)$$

with the vector of conservative variables \mathbf{Q} and the flux tensor $\underline{\mathbf{H}}$. The control volume V is enclosed by the surface $A = \partial V$, where \mathbf{n} is the outward unit normal vector on dA . The flux tensor $\underline{\mathbf{H}}$ is split into the inviscid part $\underline{\mathbf{H}}_{inv}$ and the viscous terms $\underline{\mathbf{H}}_{vis}$,

$$\mathbf{Q} = \begin{pmatrix} \rho \\ \rho \mathbf{u} \\ \rho E \\ \rho Y \end{pmatrix}, \quad \underline{\mathbf{H}}_{inv} = \begin{pmatrix} \rho \mathbf{u} \\ \rho \mathbf{u} \mathbf{u} + p \mathbf{I} \\ \mathbf{u} (\rho E) + p \mathbf{u} \\ \rho \mathbf{u} Y \end{pmatrix}, \quad \underline{\mathbf{H}}_{vis} = \frac{1}{Re_0} \begin{pmatrix} 0 \\ \underline{\boldsymbol{\tau}} \\ \underline{\boldsymbol{\tau}} \mathbf{u} + \mathbf{q} \\ J_Y \end{pmatrix}. \quad (2.2)$$

Here, ρ denotes the density, \mathbf{u} the flow velocity, E the total specific energy, p the pressure, Y the concentration of a passive scalar and $\underline{\boldsymbol{\tau}}$ the deviatoric stress tensor. An additional transport equation is solved for a passive scalar Y with the diffusive flux $J_Y = \frac{1}{Sc_0} \rho D \nabla Y$. The Schmidt number is assumed to be constant, $Sc_0 = \frac{\eta_{d,0}}{\rho_{d,0} D_{d,0}} = 1.0$, and for a constant Schmidt number the diffusion coefficient becomes $D = \eta(T)/\rho$.

All dimensional variables T_d , ρ_d , $u_{d,i}$, p_d and t_d are non-dimensionalized based on the stagnation state quantities indicated by “0”,

$$T = \frac{T_d}{T_{d,0}}, \quad \rho = \frac{\rho_d}{\rho_{d,0}}, \quad u_i = \frac{u_{d,i}}{a_{d,0}}, \quad p = \frac{p_d}{\rho_{d,0} a_{d,0}^2} \quad (2.3)$$

$$t = \frac{t_d a_{d,0}}{L_{ref,d}} \quad \text{and} \quad a_{d,0} = \sqrt{\gamma R_d T_{d,0}},$$

with the specific gas constant R_d .

The stagnation state Reynolds number Re_0 is

$$Re_0 = \frac{\rho_{d,0} a_{d,0} L_{ref,d}}{\eta_{d,0}} \quad (2.4)$$

with a_0 the speed of sound at state of rest.

The deviatoric stress tensor of a Newtonian fluid with zero bulk viscosity is defined as

$$\underline{\boldsymbol{\tau}} = -\eta (\nabla \mathbf{u} + (\nabla \mathbf{u})^\top) + \frac{2}{3} \eta (\nabla \cdot \mathbf{u}) \underline{\mathbf{I}} \quad (2.5)$$

where η is the dynamic viscosity and $\underline{\mathbf{I}}$ the unit tensor.

According to Fourier's law the heat conduction \mathbf{q} with the thermal conductivity k reads

$$\mathbf{q} = -\frac{k}{Pr_0(\gamma - 1)} \nabla T. \quad (2.6)$$

The ratio of specific heats is $\gamma = \frac{c_p}{c_v}$, where c_p is the specific heat capacity at constant pressure and c_v the specific heat capacity at constant volume. The stagnation state Prandtl number is calculated by $Pr_0 = \eta_0 c_p / k_0$. The heat conductivity and dynamic viscosity are computed by Sutherland's law,

$$k = \eta = (T)^{3/2} \frac{1 + S}{T + S}, \quad (2.7)$$

where $S = \frac{111\text{K}}{T_0}$ is the Sutherland's constant.

The thermal equation of state for a perfect caloric ideal gas reads

$$e = E - \frac{\mathbf{u}^2}{2} = \frac{p}{\rho(\gamma - 1)} \quad (2.8)$$

with the internal specific energy e .

2.2 Numerical Method

The governing equations are solved with the Zonal Flow Solver (ZFS) developed at the institute of aerodynamic at RWTH Aachen. The mathematical method to solve the Navier-Stokes equations is the LES where all length scales below a certain quantity are spatially filtered. The filter size is equal to the cell length. All scales, that are not resolved, are considered through numerical dissipation [3, 12]. ZFS uses a cell-centered, finite-volume method on an unstructured Cartesian grid. The grid is generated automatic by an efficient mesh generation parallelized for the use on high-performance computers [10].

The inviscid terms are discretized with a low-dissipation advection upstream splitting method of second order [12]. Here, the cell-surface variables are extrapolated by a monotonic upstream-centered scheme for conservation laws [19]. The amount of numerical dissipation is controlled by a reconstruction method [23]. The viscous terms are discretized by a central scheme, where the gradients at the cell surfaces are computed by a recentering-approach [2].

The conservative variables are integrated in time from t^n to $t^{n+1} = t^n + \Delta t$ with the predictor-corrector Runge-Kutta scheme of second order [19],

$$\begin{aligned} (\mathbf{Q}V)^{(0)} &= (\mathbf{Q}V)^n, \\ (\mathbf{Q}V)^{(1)} &= (\mathbf{Q}V)^{(0)} - \Delta t \mathbf{R}(t^n, \mathbf{Q}^{(0)}), \\ (\mathbf{Q}V)^{(k)} &= (\mathbf{Q}V)^{(0)} - \Delta t \left((1 - \alpha_{k-1}) \mathbf{R}(t^n, \mathbf{Q}^{(0)}) + \alpha_{k-1} \mathbf{R}(t^{n+1}, \mathbf{Q}^{(k-1)}) \right), \quad k = 2, \dots, s, \\ (\mathbf{Q}V)^{n+1} &= (\mathbf{Q}V)^{(s)}. \end{aligned} \tag{2.9}$$

The Runge-Kutta coefficients are $\alpha = (1/4 \quad 1/6 \quad 3/8 \quad 1/2 \quad 1)$, and $\mathbf{R}(t, \cdot)$ is the residual operator. The advantage of this Runge-Kutta scheme is the elimination of the intermediate time levels. The residual operator is only constructed at the time levels t^n and t^{n+1} reducing the computational cost.

Cells which intersect the boundary are cut, and treated by a small cell correction after every Runge-Kutta substage to reassure stability [19],

$$\mathbf{Q}'_c = \mathbf{Q}_c^{(k)} + (1 - \kappa_c) (\mathbf{Q}_c^i - \mathbf{Q}_c^{(k)}). \tag{2.10}$$

The Runge-Kutta substage $\mathbf{Q}_c^{(k)}$ is corrected towards an interpolated stable solution \mathbf{Q}_c^i . The parameter $\kappa_c \in [0, 1]$ is an indicator for the size of the cut cell and calculated as

$$\kappa_c = \lambda \left(2 \frac{V_c}{V} \right), \quad \lambda(r) = \begin{cases} 0 & \text{if } r < 0, \\ 3r^2 - 2r^3 & \text{if } 0 \leq r \leq 1, \\ 1 & \text{if } r > 0. \end{cases} \tag{2.11}$$

It is V_c the volume of the cut cell and V the volume of an uncut cell. The conservation is recovered by the redistribution of the mass defect \mathbf{D}_c to the cells l in the neighborhood M_c ,

$$\begin{aligned} \mathbf{D}_c &= (1 - \kappa_c) (\mathbf{Q}_c^{(k)} - \mathbf{Q}_c^i) V_c^{(k)}, \\ \mathbf{Q}_l'' &= \mathbf{Q}_l' + \sigma_{c,l} \mathbf{D}_c / V_l, \quad \forall l \in M_c \\ \sigma_{c,l} &= \frac{V_l}{\sum_{j \in M_c} V_j}. \end{aligned} \tag{2.12}$$

Details on the small cell correction and the interpolation method can be found in the work of Schneiders et al. [19].

ZFS offers a variety of in- and outflow boundary conditions. For comparison with the CBC, standard Neumann and Dirichlet type boundary conditions are used. At the inflow boundary Γ_{in} , a constant inflow velocity $u_{1,in}$ and a constant density ρ_{in} are imposed. Further, the

pressure gradient normal to the boundary is set to zero,

$$\mathbf{u}(\mathbf{x}, t) = \begin{pmatrix} u_{1,in} \\ 0 \\ 0 \end{pmatrix}, \quad \rho(\mathbf{x}, t) = \rho_{in}, \quad \frac{\partial p}{\partial n} = 0, \quad \mathbf{x} \in \Gamma_{in}. \quad (2.13)$$

At the outflow boundary Γ_{out} , a constant static pressure p_{out} is imposed while the gradients for velocity and density are set to zero,

$$p(\mathbf{x}, t) = p_{out}, \quad \frac{\partial \mathbf{u}}{\partial n} = 0, \quad \frac{\partial \rho}{\partial n} = 0, \quad \mathbf{x} \in \Gamma_{out}. \quad (2.14)$$

At fixed and at moving wall boundaries Γ_w , the no-slip condition is imposed. The pressure gradient is set to zero and all boundaries are assumed adiabatic,

$$\mathbf{u}(\mathbf{x}, t) = \mathbf{u}_w(\mathbf{x}, t), \quad \frac{\partial p}{\partial n} = 0, \quad \frac{\partial T}{\partial n} = 0, \quad \mathbf{x} \in \Gamma_w. \quad (2.15)$$

At slip walls, the velocity normal to the wall is zero, and the wall normal gradients of density, pressure and temperature are set to zero. The boundary is assumed to be adiabatic,

$$\mathbf{u}_n = 0, \quad \frac{\partial u_t}{\partial n} = \frac{\partial \rho}{\partial n} = \frac{\partial p}{\partial n} = 0, \quad \frac{\partial T}{\partial n} = 0, \quad \mathbf{x} \in \Gamma_w. \quad (2.16)$$

The gradients of the boundary conditions are imposed by a ghost cell method where cells are placed outside of the physical domain. Those cells are included into the calculation of the gradients, and their flow variables are chosen, such that the desired gradients arise between boundary cells and ghost cells [19]. The previously described inflow and outflow boundary conditions are partially reflective. In order to damp wave reflections, a sponge layer method is applied to cells with a specific distance to the inflow and outflow boundary [5].

At inflow boundaries, synthetic turbulence can be imposed. The turbulent velocity fluctuations are generated using the approach by Batten et al. [1]. This method is based on Fourier series, and returns pseudo-random fluctuations for the velocity components u'_1, u'_2 and u'_3 . These turbulent fluctuations can be added to the mean inflow velocity in Eq. (2.13) such that

$$\mathbf{u}(\mathbf{x}, t) = \begin{pmatrix} u_{1,in} + u'_1 \\ u'_2 \\ u'_3 \end{pmatrix}, \quad \mathbf{x} \in \Gamma_{in}. \quad (2.17)$$

Chapter 3

Characteristic Boundary Equations

3.1 Derivation of the Characteristic Form of the Navier-Stokes Equations

In this section, the characteristic form of the Navier-Stokes equations is derived. The divergence form of the conservation equations,

$$\frac{\partial \mathbf{Q}}{\partial t} + \nabla \cdot \mathbf{H} = 0, \quad (3.1)$$

is derived from the ALE formulation in Eq. (2.1) by applying the Gaussian integral theorem,

$$\oint_{\partial V} \mathbf{H} \cdot \mathbf{n} dA = \int_V \nabla \cdot \mathbf{H} dV, \quad (3.2)$$

and integrating for the volume V . The Jacobian matrix $\mathbf{P} = \frac{\partial \mathbf{Q}}{\partial \mathbf{V}}$ is inverted, and used to transform the conservative variables \mathbf{Q} into the primitive variables \mathbf{V} ,

$$\mathbf{V} = \begin{pmatrix} \rho \\ \mathbf{u} \\ p \\ Y \end{pmatrix}. \quad (3.3)$$

The Jacobian and its inverse are

$$\mathbf{P} = \begin{pmatrix} 1 & 0 & 0 & 0 & 0 & 0 \\ u_1 & \rho & 0 & 0 & 0 & 0 \\ u_2 & 0 & \rho & 0 & 0 & 0 \\ u_3 & 0 & 0 & \rho & 0 & 0 \\ \frac{1}{2}u_i^2 & \rho u_1 & \rho u_2 & \rho u_3 & \frac{1}{\gamma-1} & 0 \\ Y & 0 & 0 & 0 & 0 & \rho \end{pmatrix} \quad (3.4)$$

and

$$\mathbf{P}^{-1} = \begin{pmatrix} 1 & 0 & 0 & 0 & 0 & 0 \\ -u_1/\rho & 1/\rho & 0 & 0 & 0 & 0 \\ -u_2/\rho & 0 & 1/\rho & 0 & 0 & 0 \\ -u_3/\rho & 0 & 0 & 1/\rho & 0 & 0 \\ \frac{\gamma-1}{2}u_i^2 & (1-\gamma)u_1 & (1-\gamma)u_2 & (1-\gamma)u_3 & \gamma-1 & 0 \\ -Y/\rho & 0 & 0 & 0 & 0 & 1/\rho \end{pmatrix}. \quad (3.5)$$

Applying $\underline{\mathbf{P}}^{-1}$ to the conservative divergence form of the Navier-Stokes Eq. (3.1) yields the quasi-conservative form,

$$\begin{aligned} \underline{\mathbf{P}}^{-1} \frac{\partial \mathbf{Q}}{\partial t} + \underline{\mathbf{P}}^{-1} \nabla \cdot (\underline{\mathbf{H}}_{inv} + \underline{\mathbf{H}}_{vis}) &= 0, \\ \frac{\partial \mathbf{V}}{\partial t} + \underline{\mathbf{A}}_i \frac{\partial \mathbf{V}}{\partial x_i} + \mathbf{D} &= 0, \quad \text{and} \quad \mathbf{D} = \underline{\mathbf{P}}^{-1} (\nabla \cdot \underline{\mathbf{H}}_{vis}), \end{aligned} \quad (3.6)$$

where the matrix $\underline{\mathbf{A}}_i$ describes the quasi-conservative Jacobian matrix of the fluxes,

$$\underline{\mathbf{A}}_i = \begin{pmatrix} u_i & \delta_{1i}\rho & \delta_{2i}\rho & \delta_{3i}\rho & 0 & 0 \\ 0 & u_i & 0 & 0 & \delta_{1i}/\rho & 0 \\ 0 & 0 & u_i & 0 & \delta_{2i}/\rho & 0 \\ 0 & 0 & 0 & u_i & \delta_{3i}/\rho & 0 \\ 0 & \delta_{1i}\gamma p & \delta_{2i}\gamma p & \delta_{3i}\gamma p & u_i & 0 \\ 0 & 0 & 0 & 0 & 0 & u_i \end{pmatrix}. \quad (3.7)$$

Here, δ_{ji} is the Kronecker's delta,

$$\delta_{ij} = \begin{cases} 0 & \text{if } i \neq j, \\ 1 & \text{if } i = j. \end{cases} \quad (3.8)$$

The eigenvalues λ_{ik} of the tensors $\underline{\mathbf{A}}_i$ can be calculated from the determinant $\det(\underline{\mathbf{A}}_i - \lambda_{ik}\underline{\mathbf{I}}) = 0$. The quasi-conservative Jacobian matrix can be diagonalized by

$$\underline{\mathbf{A}}_i = \underline{\mathbf{T}}_i^{-1} \underline{\mathbf{A}}_i \underline{\mathbf{T}}_i = \begin{pmatrix} \lambda_{i1} \\ \lambda_{i2} \\ \lambda_{i3} \\ \lambda_{i4} \\ \lambda_{i5} \\ \lambda_{i6} \end{pmatrix} \underline{\mathbf{I}} = \begin{pmatrix} u_i - a \\ u_i \\ u_i \\ u_i \\ u_i + a \\ u_i \end{pmatrix} \underline{\mathbf{I}} \quad (3.9)$$

with the eigenvector matrix $\underline{\mathbf{T}}_i = (\mathbf{t}_{i1} \ \mathbf{t}_{i2} \ \mathbf{t}_{i3} \ \mathbf{t}_{i4} \ \mathbf{t}_{i5} \ \mathbf{t}_{i6})$ calculated from

$$(\underline{\mathbf{A}}_i - \lambda_{ik}\underline{\mathbf{I}}) \mathbf{t}_{ik} = 0. \quad (3.10)$$

The eigenvalue matrix and its inverse read

$$\underline{\mathbf{T}}_i = \begin{pmatrix} 1/(2a^2) & \delta_{1i}/a^2 & \delta_{2i}/a^2 & \delta_{3i}a^2 & 1/(2a^2) & 0 \\ -\delta_{1i}/(2\rho a) & 1 - \delta_{1i} & 0 & 0 & \delta_{1i}/(2\rho a) & 0 \\ -\delta_{2i}/(2\rho a) & 0 & 1 - \delta_{2i} & 0 & \delta_{2i}/(2\rho a) & 0 \\ -\delta_{3i}/(2\rho a) & 0 & 0 & 1 - \delta_{3i} & \delta_{3i}/(2\rho a) & 0 \\ 1/2 & 0 & 0 & 0 & 1/2 & 0 \\ 0 & 0 & 0 & 0 & 0 & 1 \end{pmatrix} \quad (3.11)$$

and

$$\underline{\mathbf{T}}_i^{-1} = \begin{pmatrix} 0 & -\delta_{1i}\rho a & -\delta_{2i}\rho a & -\delta_{3i}\rho a & 1 & 0 \\ \delta_{1i}a^2 & 1 - \delta_{1i} & 0 & 0 & -\delta_{1i} & 0 \\ \delta_{2i}a^2 & 0 & 1 - \delta_{2i} & 0 & -\delta_{2i} & 0 \\ \delta_{3i}a^2 & 0 & 0 & 1 - \delta_{3i} & -\delta_{3i} & 0 \\ 0 & \delta_{1i}\rho a & \delta_{2i}\rho a & \delta_{3i}\rho a & 1 & 0 \\ 0 & 0 & 0 & 0 & 0 & 1 \end{pmatrix}. \quad (3.12)$$

Finally, the diagonalized characteristic formulation reads

$$\frac{\partial}{\partial t} \mathbf{V} + \underline{\mathbf{T}}_i \underline{\mathbf{A}}_i \underline{\mathbf{T}}_i^{-1} \frac{\partial}{\partial x_i} \mathbf{V} + \mathbf{D} = 0. \quad (3.13)$$

3.2 Derivation of the LODI and the 3D-NSCBC System

The Local One-Dimensional Inviscid (LODI) system is derived from the diagonalized characteristic formulation in Eq. (3.13) by neglecting the tangential and viscous terms,

$$\frac{\partial}{\partial t} \mathbf{V} + \underbrace{\mathbf{T}_1 \mathbf{A}_1 \mathbf{T}_1^{-1} \frac{\partial}{\partial x_1} \mathbf{V}}_{\mathcal{L}} + \underbrace{\mathbf{A}_2 \frac{\partial}{\partial x_2} \mathbf{V} + \mathbf{A}_3 \frac{\partial}{\partial x_2} \mathbf{V}}_{\text{tangential terms}} + \underbrace{\mathbf{B}^0}_{\text{viscous terms}} = 0. \quad (3.14)$$

Thompson [22] defined the vector \mathcal{L} which contains the amplitude wave variations,

$$\mathcal{L} = (\mathcal{L}_1 \quad \mathcal{L}_2 \quad \mathcal{L}_3 \quad \mathcal{L}_4 \quad \mathcal{L}_5 \quad \mathcal{L}_6)^\top. \quad (3.15)$$

Multiplying the eigenvalue matrix \mathbf{T}_1 with the amplitude wave variations \mathcal{L} results in

$$\mathbf{d} = \mathbf{T}_1 \mathcal{L} = \begin{pmatrix} \frac{1}{a^2} (\mathcal{L}_2 + \frac{1}{2} (\mathcal{L}_5 + \mathcal{L}_1)) \\ \frac{1}{2\rho a} (\mathcal{L}_5 - \mathcal{L}_1) \\ \mathcal{L}_3 \\ \mathcal{L}_4 \\ \frac{1}{2} (\mathcal{L}_5 + \mathcal{L}_1) \\ \mathcal{L}_6 \end{pmatrix}. \quad (3.16)$$

Inserting in Eq. (3.14) gives the LODI system [22, 16],

$$\frac{\partial}{\partial t} \mathbf{V} + \mathbf{d} = 0. \quad (3.17)$$

The LODI and the 3D-NSCBC formulations describe the flow as waves crossing the boundaries. The terms \mathcal{L}_k can be interpreted as wave amplitude variations of acoustic, convective and entropy waves in the x_1 -direction [16]. Because of the characteristic formulation along the normal direction of the boundary, all incoming and outgoing waves can be separated as shown in Fig. 3.1 which shows all characteristic waves entering and leaving the domain. Here, waves with eigenvalues $\lambda_{1k} > 0$ at $x_1 = -L/2$ and $\lambda_{1k} < 0$ at $x_1 = L/2$ are entering the computational domain, while waves with eigenvalues $\lambda_{1k} \leq 0$ at $x_1 = -L/2$ and $\lambda_{1k} \geq 0$ at $x_1 = L/2$ are leaving the computational domain [16]. Outgoing waves can be directly calculated by the information inside of the computational domain as

$$\mathcal{L} = \mathbf{A}_1 \mathbf{T}_1^{-1} \frac{\partial}{\partial x_1} \mathbf{V} = \begin{pmatrix} \lambda_{11} \left(\frac{\partial p}{\partial x_1} - \rho a \frac{\partial u_1}{\partial x_1} \right) \\ \lambda_{12} \left(a^2 \frac{\partial \rho}{\partial x_1} - \frac{\partial p}{\partial x_1} \right) \\ \lambda_{13} \frac{\partial u_2}{\partial x_1} \\ \lambda_{14} \frac{\partial u_3}{\partial x_1} \\ \lambda_{15} \left(\frac{\partial p}{\partial x_1} + \rho a \frac{\partial u_1}{\partial x_1} \right) \\ \lambda_{16} \frac{\partial Y}{\partial x_1} \end{pmatrix}. \quad (3.18)$$

For characteristic waves entering the domain, a meaningful expression needs to be prescribed accounting for all information propagating into the domain.

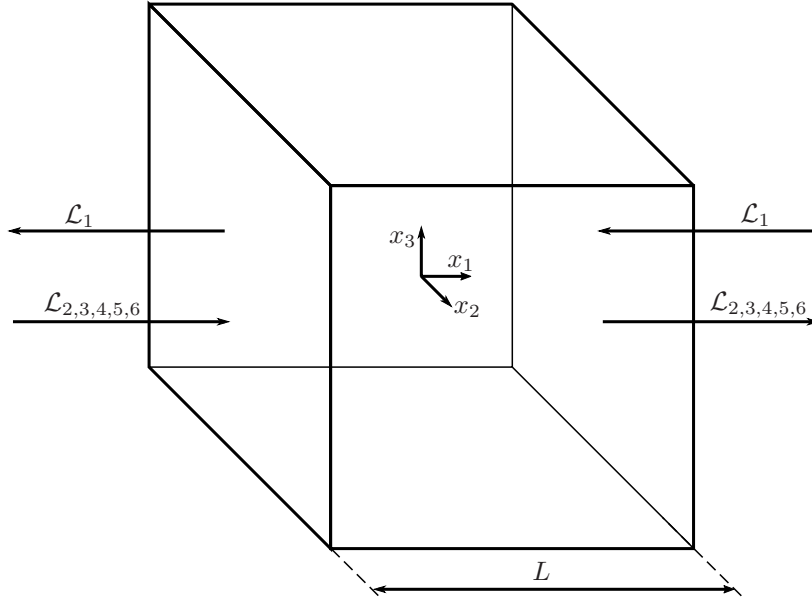


Figure 3.1: Characteristic waves leaving and entering the computational domain [16].

For unidirectional, inviscid flows normal to the boundary, the LODI system is a valid assumption [16]. In case of a strong rotational flow, as for example in turbomachinery, the tangential terms describing the rotational motion can, however, not be neglected [25, 9]. In this case, the LODI system needs to be extended by the 3D-NSCBC approach as described by Yoo et al. [25, 24] and Lodato et al. [11]. The 3D-NSCBC equation system is obtained by considering the tangential terms \mathcal{T} and the viscous terms \mathcal{D} in Eq. (3.13) as

$$\frac{\partial}{\partial t} \mathbf{V} + \mathbf{d} + \underbrace{\mathbf{A}_2 \frac{\partial}{\partial x_2} \mathbf{V} + \mathbf{A}_3 \frac{\partial}{\partial x_3} \mathbf{V}}_{-\mathcal{T}} + \underbrace{\mathbf{D}}_{-\mathcal{D}} = 0. \quad (3.19)$$

The tangential terms can be directly calculated from the flow variables inside of the computational domain as

$$\mathcal{T} = -\mathbf{A}_2 \frac{\partial \mathbf{V}}{\partial x_2} - \mathbf{A}_3 \frac{\partial \mathbf{V}}{\partial x_3} = \begin{pmatrix} -\frac{\partial(\rho u)_2}{\partial x_2} - \frac{\partial(\rho u)_3}{\partial x_3} \\ -u_2 \frac{\partial u_1}{\partial x_2} - u_3 \frac{\partial u_1}{\partial x_3} \\ -u_2 \frac{\partial u_2}{\partial x_2} - \frac{1}{\rho} \frac{\partial p}{\partial x_2} - u_3 \frac{\partial u_2}{\partial x_3} \\ -u_2 \frac{\partial u_3}{\partial x_2} - \frac{1}{\rho} \frac{\partial p}{\partial x_3} - u_3 \frac{\partial u_3}{\partial x_3} \\ -u_2 \frac{\partial p}{\partial x_2} - \gamma p \frac{\partial u_2}{\partial x_2} - u_3 \frac{\partial p}{\partial x_3} - \gamma p \frac{\partial u_3}{\partial x_3} \\ -u_2 \frac{\partial Y}{\partial x_2} - u_3 \frac{\partial Y}{\partial x_3} \end{pmatrix}. \quad (3.20)$$

By following Eq. (3.6), the viscous terms can be written as

$$\mathcal{D} = -\underline{\mathbf{P}}^{-1} (\nabla \cdot \underline{\mathbf{H}}_{vis}) = - \begin{pmatrix} 0 \\ \frac{1}{\rho Re_0} \left(\frac{\partial \tau_{11}}{\partial x_1} + \frac{\partial \tau_{12}}{\partial x_2} + \frac{\partial \tau_{13}}{\partial x_3} \right) \\ \frac{1}{\rho Re_0} \left(\frac{\partial \tau_{21}}{\partial x_1} + \frac{\partial \tau_{22}}{\partial x_2} + \frac{\partial \tau_{23}}{\partial x_3} \right) \\ \frac{1}{\rho Re_0} \left(\frac{\partial \tau_{31}}{\partial x_1} + \frac{\partial \tau_{32}}{\partial x_2} + \frac{\partial \tau_{33}}{\partial x_3} \right) \\ D_5 \\ \frac{1}{\rho Re_0} \left(\frac{\partial J_Y}{\partial x_1} + \frac{\partial J_Y}{\partial x_2} + \frac{\partial J_Y}{\partial x_3} \right) \end{pmatrix} \quad (3.21)$$

with

$$\begin{aligned} D_5 = & \frac{\gamma - 1}{Re_0} \left[\tau_{11} \frac{\partial u_1}{\partial x_1} + \tau_{22} \frac{\partial u_2}{\partial x_2} + \tau_{33} \frac{\partial u_3}{\partial x_3} + \tau_{12} \left(\frac{\partial u_2}{\partial x_1} + \frac{\partial u_1}{\partial x_2} \right) \right. \\ & \left. + \tau_{13} \left(\frac{\partial u_3}{\partial x_1} + \frac{\partial u_1}{\partial x_3} \right) + \tau_{23} \left(\frac{\partial u_3}{\partial x_2} + \frac{\partial u_2}{\partial x_3} \right) + \frac{\partial q_1}{\partial x_1} + \frac{\partial q_2}{\partial x_2} + \frac{\partial q_3}{\partial x_3} \right]. \end{aligned} \quad (3.22)$$

Lodato et al. [11] discussed the need for a special treatment of edges and corners where CBC intersect. In this thesis, the CBC only intersect with the ghost cell boundary conditions described in section 2.2. Since the ghost cells are included in the calculation of the tangential and viscous terms, there is no need for a special treatment of edges and corners. In case the tangential and viscous terms are neglected, the ghost cell type boundaries are not considered at corner and edge cells of the CBC.

The boundary conditions are time dependent. Since the conservation equations are solved in conservative form, Eq. (3.19) has to be recast into the conservative form by applying the Jacobian tensor $\underline{\mathbf{P}}$ [16],

$$\begin{aligned} \frac{\partial}{\partial t} \mathbf{V} + \mathbf{d} + \underline{\mathbf{A}}_2 \frac{\partial}{\partial x_2} \mathbf{V} + \underline{\mathbf{A}}_3 \frac{\partial}{\partial x_3} \mathbf{V} + \mathbf{D} &= 0, \\ \frac{\partial}{\partial t} \mathbf{Q} + \underline{\mathbf{P}} \mathbf{d} + \underline{\mathbf{P}} \underline{\mathbf{A}}_2 \frac{\partial}{\partial x_2} \mathbf{V} + \underline{\mathbf{P}} \underline{\mathbf{A}}_3 \frac{\partial}{\partial x_3} \mathbf{V} + \underline{\mathbf{P}} \mathbf{D} &= 0. \end{aligned} \quad (3.23)$$

Eq. (3.23) are valid for both, the LODI system and the 3D-NSCBC system. Eq. (3.23) can also be expressed by the tangential terms and viscous terms as

$$\frac{\partial \mathbf{V}}{\partial t} = \mathbf{RHS} = -\mathbf{d} + \mathcal{T} + \mathcal{D}. \quad (3.24)$$

Finally, the residual $\frac{\partial \mathbf{Q}}{\partial t}$ can be calculated which is the right hand side used in the time

integration of the solver,

$$\frac{\partial \mathbf{Q}}{\partial t} = \mathbf{P} \mathbf{RHS}, \quad (3.25)$$

$$\frac{\partial \mathbf{Q}}{\partial t} = \begin{pmatrix} RHS_1 \\ u_1 RHS_1 + \rho RHS_2 \\ u_2 RHS_1 + \rho RHS_3 \\ u_3 RHS_1 + \rho RHS_4 \\ \frac{1}{2}u_i^2 RHS_1 + \rho u_1 RHS_2 + \rho u_2 RHS_3 + \rho u_3 RHS_4 + \frac{1}{\gamma-1} RHS_5 \\ Y RHS_1 + \rho RHS_6 \end{pmatrix}. \quad (3.26)$$

3.3 Different Formulations of the 3D-NSCBC System

The 3D-NSCBC system can be cast in multiple forms in terms of different variables prescribed at the boundary or used for the derivation of the CBC. The 3D-NSCBC formulations, used in this thesis, are presented in the following.

Primitive Variables

The 3D-NSCBC form of the primitive variables \mathbf{V} is given by [22, 16]

$$\begin{aligned} & \frac{\partial \mathbf{V}}{\partial t} + \mathbf{d} - \mathcal{T} - \mathcal{D} = 0, \\ & \begin{pmatrix} \frac{\partial \rho}{\partial t} + \frac{1}{a^2} (\mathcal{L}_2 + \frac{1}{2} (\mathcal{L}_5 + \mathcal{L}_1)) - \mathcal{T}_1 \\ \frac{\partial u_1}{\partial t} + \frac{1}{2\rho a} (\mathcal{L}_5 - \mathcal{L}_1) - \mathcal{T}_2 - \mathcal{D}_2 \\ \frac{\partial u_2}{\partial t} + \mathcal{L}_3 - \mathcal{T}_3 - \mathcal{D}_3 \\ \frac{\partial u_3}{\partial t} + \mathcal{L}_4 - \mathcal{T}_4 - \mathcal{D}_4 \\ \frac{\partial p}{\partial t} + \frac{1}{2} (\mathcal{L}_5 + \mathcal{L}_1) - \mathcal{T}_5 - \mathcal{D}_5 \\ \frac{\partial Y}{\partial t} + \mathcal{L}_6 - \mathcal{T}_6 - \mathcal{D}_6 \end{pmatrix} = 0. \end{aligned} \quad (3.27)$$

Characteristic Variables

Reorganizing to separate the characteristic variables leads to [22, 21, 25, 24, 11]

$$\begin{aligned} & \underline{\mathbf{T}}_1^{-1} \frac{\partial \mathbf{V}}{\partial t} + \underline{\mathbf{T}}_1^{-1} \mathbf{d} - \underline{\mathbf{T}}_1^{-1} \mathcal{T} + \underline{\mathbf{T}}_1^{-1} \mathcal{D} = 0, \\ & \begin{pmatrix} \left(\frac{\partial p}{\partial t} - \rho a \frac{\partial u_1}{\partial t} \right) + \mathcal{L}_1 - (\mathcal{T}_5 - \rho a \mathcal{T}_2) - (\mathcal{D}_5 - \rho a \mathcal{D}_2) \\ \left(a^2 \frac{\partial \rho}{\partial t} - \frac{\partial p}{\partial t} \right) + \mathcal{L}_2 - (a^2 \mathcal{T}_1 - \mathcal{T}_5) + \mathcal{D}_5 \\ \frac{\partial u_2}{\partial t} + \mathcal{L}_3 - \mathcal{T}_3 - \mathcal{D}_3 \\ \frac{\partial u_3}{\partial t} + \mathcal{L}_4 - \mathcal{T}_4 - \mathcal{D}_4 \\ \left(\frac{\partial p}{\partial t} + \rho a \frac{\partial u_1}{\partial t} \right) + \mathcal{L}_5 - (\mathcal{T}_5 + \rho a \mathcal{T}_2) - (\mathcal{D}_5 + \rho a \mathcal{D}_2) \end{pmatrix} = 0. \end{aligned} \quad (3.28)$$

Static Temperature

The time derivative of the static temperature as a function of the wave amplitude variations is obtained using the ideal gas equation and the quotient rule,

$$T = \frac{\gamma p}{\rho}, \quad (3.29)$$

$$\frac{\partial T}{\partial t} = \frac{\rho \gamma \frac{\partial p}{\partial t} - \gamma p \frac{\partial \rho}{\partial t}}{\rho^2} = \frac{1}{\rho} \left(\gamma \frac{\partial p}{\partial t} - a^2 \frac{\partial \rho}{\partial t} \right). \quad (3.30)$$

By replacing the time derivatives of pressure and density with help of the 3D-NSCBC system in terms of primitive variables in Eq. (3.27), the following form is derived [16],

$$\begin{aligned} \frac{\partial T}{\partial t} &= \frac{1}{\rho} \left(\mathcal{L}_2 - \frac{1}{2} (\gamma - 1) (\mathcal{L}_5 + \mathcal{L}_1) \right) + \underbrace{\frac{1}{\rho} (\gamma \mathcal{C}_5 - a^2 \mathcal{C}_1)}_{\mathcal{C}_T}, \\ \frac{\partial T}{\partial t} &= \underbrace{\mathcal{L}_2}_{F_2} \underbrace{\frac{1}{\rho}}_{F_2} - \underbrace{\mathcal{L}_5}_{F_5} \underbrace{\frac{\gamma - 1}{2\rho}}_{F_5} - \underbrace{\mathcal{L}_1}_{F_5} \underbrace{\frac{\gamma - 1}{2\rho}}_{F_5} + \mathcal{C}_T. \end{aligned} \quad (3.31)$$

Here \mathcal{C}_i is $\mathcal{T}_i + \mathcal{D}_i$.

Kinetic Energy

A 3D-NSCBC formulation for the kinetic energy is derived by applying the chain rule on the kinetic energy e_c ,

$$\begin{aligned} e_c &= \frac{u_1^2 + u_2^2 + u_3^2}{2}, \\ \frac{\partial e_c}{\partial t} &= u_1 \frac{\partial u_1}{\partial t} + u_2 \frac{\partial u_2}{\partial t} + u_3 \frac{\partial u_3}{\partial t}. \end{aligned} \quad (3.32)$$

The time derivatives $\frac{\partial u_i}{\partial t}$ are substituted by the corresponding 3D-NSCBC Eq. (3.27) [13],

$$\frac{\partial e_c}{\partial t} = -u_1 \left(\frac{1}{2\rho a} (\mathcal{L}_5 - \mathcal{L}_1) \right) - u_2 \mathcal{L}_3 - u_3 \mathcal{L}_4 + \underbrace{u_1 \mathcal{C}_2 + u_2 \mathcal{C}_3 + u_3 \mathcal{C}_4}_{\mathcal{C}_e}. \quad (3.33)$$

Square Mach Number

The square Mach number can be represented by the kinetic energy and the static temperature. By applying the quotient rule, the time derivative of the square Mach number is obtained,

$$M^2 = \frac{u_1^2 + u_2^2 + u_3^2}{T} = \frac{2e_c}{T}, \quad (3.34)$$

$$\frac{\partial M^2}{\partial t} = \frac{2}{a^2} \left(\frac{\partial e_c}{\partial t} - \frac{e_c}{T} \frac{\partial T}{\partial t} \right). \quad (3.35)$$

Inserting the 3D-NSCBC formulations for the kinetic energy in Eq. (3.33) and the static temperature in Eq. (3.31) into Eq. (3.35) leads to [13]

$$\begin{aligned} \frac{\partial M^2}{\partial t} = \frac{2}{T} \left(\mathcal{L}_5 \left(\frac{(\gamma-1)e_c}{2\rho T} - \frac{u_1}{2\rho a} \right) + \mathcal{L}_1 \left(\frac{(\gamma-1)e_c}{2\rho T} + \frac{u_1}{2\rho a} \right) - u_2 \mathcal{L}_3 - u_3 \mathcal{L}_4 - \frac{e_c}{\rho T} \mathcal{L}_2 \right) \\ + \underbrace{\frac{2}{T} \mathcal{C}_e - \frac{2e_c}{T^2} \mathcal{C}_T}_{\mathcal{C}_M}. \end{aligned} \quad (3.36)$$

Total Pressure

Starting from the isentropic relation of total and static pressure, the 3D-NSCBC formulation for total pressure is derived. The static pressure and square Mach number derivatives are substituted by their 3D-NSCBC expression in Eq. (3.27) and Eq. (3.36) [13],

$$p_t = p \left(1 + \frac{\gamma-1}{2} M^2 \right)^{\left(\frac{\gamma}{\gamma-1} \right)}, \quad (3.37)$$

$$\frac{\partial p_t}{\partial t} = \frac{\partial p}{\partial t} \left(1 + \frac{\gamma-1}{2} M^2 \right)^{\frac{\gamma}{\gamma-1}} + p \frac{\gamma}{2} \frac{\partial M^2}{\partial t} \left(1 + \frac{\gamma-1}{2} M^2 \right)^{\left(\frac{\gamma}{\gamma-1} - 1 \right)}, \quad (3.38)$$

$$\frac{\partial p_t}{\partial t} = \frac{p_t}{p} \frac{\partial p}{\partial t} + \frac{\gamma p_t T}{2 T_t} \frac{\partial M^2}{\partial t}, \quad (3.39)$$

$$\begin{aligned} \frac{\partial p_t}{\partial t} = \underbrace{\mathcal{L}_5 \left(-\frac{1}{2} \frac{p_t}{p} + \frac{\gamma p_t}{T_t} \left(\frac{(\gamma-1)e_c}{2\rho T} - \frac{u_1}{2\rho a} \right) \right)}_{F_4} + \underbrace{\mathcal{L}_1 \left(-\frac{1}{2} \frac{p_t}{p} + \frac{\gamma p_t}{T_t} \left(\frac{(\gamma-1)e_c}{2\rho T} + \frac{u_1}{2\rho a} \right) \right)}_{F_6} \\ - \frac{\gamma p_t}{T_t} \underbrace{(u_2 \mathcal{L}_3 + u_3 \mathcal{L}_4)}_{F_3} - \mathcal{L}_2 \underbrace{\frac{e_c}{\rho T} \frac{\gamma p_t}{T_t}}_{F_1} + \underbrace{\left(\frac{p_t}{p} \mathcal{C}_5 + \frac{\gamma p_t T}{2 T_t} \mathcal{C}_M \right)}_{\mathcal{C}_{pt}}. \end{aligned} \quad (3.40)$$

Total Temperature

Analogue to the total pressure formulation, the 3D-NSCBC formulation for the total temperature is derived from the isentropic relation between total and static temperature. The quotient rule is applied. Finally, the static temperature derivative in Eq. (3.31) and the square Mach number derivative in Eq. (3.36) are inserted [13],

$$\frac{T_t}{T} = \left(1 + \frac{(\gamma - 1)}{2} M^2 \right), \quad (3.41)$$

$$\frac{\partial T_t}{\partial t} = \frac{\partial T}{\partial t} \frac{T_t}{T} + T \frac{(\gamma - 1)}{2} \frac{\partial M^2}{\partial t}, \quad (3.42)$$

$$\begin{aligned} \frac{\partial T_t}{\partial t} = & \underbrace{\mathcal{L}_5 \left(-\frac{(\gamma - 1) T_t}{2\rho T} + (\gamma - 1) \left(\frac{(\gamma - 1) e_c}{2\rho T} - \frac{u_1}{2\rho a} \right) \right)}_{F_{5T}} \\ & + \underbrace{\mathcal{L}_1 \left(-\frac{(\gamma - 1) T_t}{2\rho T} + (\gamma - 1) \left(\frac{(\gamma - 1) e_c}{2\rho T} + \frac{u_1}{2\rho a} \right) \right)}_{F_{7T}} - (\gamma - 1) \underbrace{(u_2 \mathcal{L}_3 + u_3 \mathcal{L}_4)}_{F_3} \\ & + \underbrace{\mathcal{L}_2 \left(\frac{T_t}{\rho T} - \frac{(\gamma - 1) e_c}{\rho T} \right)}_{F_{2T}} + \underbrace{\left(\frac{T_t}{T} \mathcal{C}_T + \frac{(\gamma - 1) T}{2} \mathcal{C}_M \right)}_{\mathcal{C}_{Tt}}. \end{aligned} \quad (3.43)$$

A derivation of total pressure and total temperature formulations without tangential and viscous terms can be found in Odier et al. [13].

3.4 Derivation of the Wave Amplitude Variations for Different Boundary Conditions

Partially Non-Reflecting Inflow CBC Imposing Velocity and Static Temperature

Based on the linearization of the Navier-Stokes equations, a partially non-reflecting boundary condition imposing velocity $u_{i,in}$ and static temperature T_{in} can be derived as [4]

$$\begin{aligned} \left(\frac{\partial p}{\partial t} + \zeta \rho a \frac{\partial u_1}{\partial t} \right) + \eta_\Phi (u_1 - u_{1,in}) &= 0, \\ \left(a^2 \frac{\partial \rho}{\partial t} - \frac{\partial p}{\partial t} \right) + \eta_2 (T - T_{in}) &= 0, \\ \frac{\partial u_2}{\partial t} + \eta_3 (u_2 - u_{2,in}) &= 0, \\ \frac{\partial u_3}{\partial t} + \eta_4 (u_3 - u_{3,in}) &= 0, \\ \frac{\partial Y}{\partial t} + \eta_6 (Y - Y_{in}) &= 0. \end{aligned} \quad (3.44)$$

Depending on the direction of the characteristics, the index Φ is set such that $\Phi \in \{1, 5\}$ equals the index of the wave amplitude variation coming from outside of the computational

domain. These wave amplitude variations are calculated by the boundary condition, and the wave amplitude variation in opposite direction is calculated from the information inside of the domain. Which characteristics are entering or leaving the computational domain is determined by the eigenvalues as discussed in section 3.2. The term ζ controls the sign of the characteristic variables in Eq. (3.44) [11],

$$\zeta = \frac{\Phi - 1}{2} - 1, \quad \Phi \in \{1, 5\}. \quad (3.45)$$

The η_k -terms are relaxation coefficients which control the permeability of the boundary for outgoing waves. For high values of $|\eta_k| \rightarrow \infty$, the prescribed mean values are fixed on the boundary. In case of $\eta_k = 0$, the waves can pass the boundary without being disturbed, but no target value can be imposed at the boundary. Therefore, for small values of η_k , the solution drifts or takes a long time to converge to the target value. Since both described effects are desirable, there has to be an optimal value between 0 and ∞ where, after the waves cross the boundary, the prescribed values are restored. These optimal coefficients have been approximated by Yoo et al. [25] as

$$\begin{aligned} \eta_\Phi &= \eta_\Phi^* \frac{\rho a^2 (1 - M_{max}^2)}{L}, \\ \eta_2 &= \eta_2^* \frac{\rho a}{\gamma L}, \\ \eta_{3,4,6} &= \eta_{3,4,6}^* \frac{a}{L}. \end{aligned} \quad (3.46)$$

Here, M_{max} is the maximum Mach number at the boundary, and the coefficients for $\boldsymbol{\eta}^*$ equal

$$\boldsymbol{\eta}^* = (-0.278 \quad -0.278 \quad 0.278 \quad 0.278 \quad 0.278 \quad 0.278). \quad (3.47)$$

Combining Eq. (3.28), (3.44) and (3.46) leads to the formulation of the unknown wave amplitudes [25, 24],

$$\begin{aligned} \mathcal{L}_\Phi(\mathbf{x}, t) &= \eta_\Phi^* \frac{\rho a^2 (1 - M_{max}^2)}{L} (u_1 - u_{1,in}) + (\mathcal{T}_5 + \zeta \rho a \mathcal{T}_2) + (D_5 + \zeta \rho a D_2), \\ \mathcal{L}_2(\mathbf{x}, t) &= \eta_2^* \frac{\rho a}{\gamma L} (T - T_{in}) + (a^2 \mathcal{T}_1 - \mathcal{T}_5) - D_5, \\ \mathcal{L}_3(\mathbf{x}, t) &= \eta_3^* \frac{a}{L} (u_2 - u_{2,in}) + \mathcal{T}_3 + D_3, \\ \mathcal{L}_4(\mathbf{x}, t) &= \eta_4^* \frac{a}{L} (u_3 - u_{3,in}) + \mathcal{T}_4 + D_4, \\ \mathcal{L}_6(\mathbf{x}, t) &= \eta_6^* \frac{a}{L} (Y - Y_{in}) + \mathcal{T}_6 + D_6, \quad \mathbf{x} \in \Gamma_{in}. \end{aligned} \quad (3.48)$$

Partially Non-Reflecting Outflow CBC Imposing Static Pressure

A partially non-reflecting outflow boundary condition, imposing the static pressure p_{out} , is derived similar as the non-reflecting inflow boundary condition [4, 25],

$$\left(\frac{\partial p}{\partial t} + \zeta \rho a \frac{\partial u}{\partial t} \right) = -\sigma (p - p_{out}) + \beta (\mathcal{T}_5 + \zeta \rho a \mathcal{T}_2). \quad (3.49)$$

The term multiplied with β is a transverse damping term necessary to stabilize the solution [25]. The transverse damping parameter $\beta = \langle M \rangle_{\mathbf{x}}$, $\mathbf{x} \in \Gamma_{out}$ is chosen as mean Mach number at the outflow boundary [7]. The relaxation coefficient is calculated as

$$\sigma = \sigma^* \frac{a(1 - M_{max}^2)}{L} \quad (3.50)$$

with an estimation of the optimal relaxation coefficient, $\sigma^* = 0.25$ [18].

The following viscous conditions are used [16, 11],

$$\frac{\partial q_1}{\partial x_1} = 0, \quad \frac{\partial \tau_{12}}{\partial x_1} = 0, \quad \frac{\partial \tau_{13}}{\partial x_1} = 0, \quad \frac{\partial J_Y}{\partial x_1} = 0. \quad (3.51)$$

Combining Eq. (3.28), (3.49) and (3.50) leads to [25, 24]

$$\mathcal{L}_\Phi(\mathbf{x}, t) = \sigma^* \frac{a(1 - M_{max}^2)}{L} (p - p_{out}) + (1 - \beta) (\mathcal{T}_5 + \zeta \rho a \mathcal{T}_2) + (\mathcal{D}_5 + \zeta \rho a \mathcal{D}_2), \quad \mathbf{x} \in \Gamma_{out}. \quad (3.52)$$

Instead of using the local pressure p in every boundary cell to impose the target pressure p_{out} , it is possible to use the at the boundary spatially averaged pressure $\langle p \rangle_{\mathbf{x}}$, $\mathbf{x} \in \Gamma_{out}$. The pressure profile of the outflow boundary can fit to the pressure distribution inside the computational domain, and only the spatial average of the pressure is imposed. This is referred to as the patch-averaged formalism [9],

$$\mathcal{L}_\Phi(\mathbf{x}, t) = \sigma^* \frac{a(1 - M_{max}^2)}{L} (\langle p \rangle_{\mathbf{x}} - p_{out}) + (1 - \beta) (\mathcal{T}_5 + \zeta \rho a \mathcal{T}_2) + (\mathcal{D}_5 + \zeta \rho a \mathcal{D}_2), \quad \mathbf{x} \in \Gamma_{out}. \quad (3.53)$$

Partially Non-Reflecting Inflow CBC Imposing Total Pressure, Total Temperature and Tangential Velocities

The wave amplitude variations, imposing the total pressure $p_{t,in}$, the total temperature $T_{t,in}$ and the to the boundary tangential velocities $u_{2,in}$ and $u_{3,in}$, can be derived by solving the following equation system, containing the 3D-NSCBC expressions for total pressure in Eq. (3.40), total temperature in Eq. (3.43) and tangential velocities in Eq. (3.27). This CBC has been derived by Odier et al. [13],

$$\begin{cases} \mathcal{L}_5 \cdot F_4 - \mathcal{L}_2 F_1 = \frac{\partial p_t}{\partial t} + \frac{\gamma p_t}{T_t} F_3 - \mathcal{L}_1 \cdot F_6 - \mathcal{C}_{pt}, \\ \mathcal{L}_5 \cdot F_{5T} + \mathcal{L}_2 F_{2T} = \frac{\partial T_t}{\partial t} + (\gamma - 1) F_3 - \mathcal{L}_1 \cdot F_{7T} - \mathcal{C}_{Tt}, \\ \frac{\partial u_2}{\partial t} = -\mathcal{L}_3 + \mathcal{C}_3 \\ \frac{\partial u_3}{\partial t} = -\mathcal{L}_4 + \mathcal{C}_4 \\ \frac{\partial Y}{\partial t} = -\mathcal{L}_6 + \mathcal{C}_6. \end{cases} \quad (3.54)$$

It is

$$\begin{aligned}
F_1 &= \frac{e_c}{\rho T} \frac{\gamma p_t}{T_t}, \\
F_{2T} &= \left(\frac{T_t}{\rho T} - \frac{(\gamma - 1) e_c}{\rho T} \right), \\
F_3 &= u_2 \mathcal{L}_3 + u_3 \mathcal{L}_4, \\
F_4 &= \left(-\frac{1}{2} \frac{p_t}{p} + \frac{\gamma p_t}{T_t} \left(\frac{(\gamma - 1) e_c}{2 \rho T} - \frac{u_1}{2 \rho a} \right) \right), \\
F_{5T} &= \left(-\frac{(\gamma - 1) T_t}{2 \rho T} + (\gamma - 1) \left(\frac{(\gamma - 1) e_c}{2 \rho T} - \frac{u_1}{2 \rho a} \right) \right), \\
F_6 &= \left(-\frac{1}{2} \frac{p_t}{p} + \frac{\gamma p_t}{T_t} \left(\frac{(\gamma - 1) e_c}{2 \rho T} + \frac{u_1}{2 \rho a} \right) \right), \\
F_{7T} &= \left(-\frac{(\gamma - 1) T_t}{2 \rho T} + (\gamma - 1) \left(\frac{(\gamma - 1) e_c}{2 \rho T} + \frac{u_1}{2 \rho a} \right) \right).
\end{aligned} \tag{3.55}$$

The equation system is solved two times for different unknown variables. In case \mathcal{L}_1 is coming from outside of the domain, \mathcal{L}_5 is calculated from variables inside of the domain and the equation system is solved for $\mathcal{L}_1, \mathcal{L}_2, \mathcal{L}_3, \mathcal{L}_4$ and \mathcal{L}_6 . For the second case \mathcal{L}_5 is unknown, and the system is solved for $\mathcal{L}_2, \mathcal{L}_3, \mathcal{L}_4, \mathcal{L}_5$ and \mathcal{L}_6 .

The solved equation system reads

$$\begin{aligned}
\mathcal{L}_1(\mathbf{x}, t) &= \frac{\frac{\partial T_t}{\partial t} F_1 + \frac{\partial p_t}{\partial t} F_{2T} + \frac{\gamma p_t}{T_t} F_3 F_{2T} + \kappa F_3 F_1 - \mathcal{L}_5 (F_4 F_{2T} + F_{5T} F_1) - \mathcal{C}_{pt} F_{2T} - \mathcal{C}_{Tt} F_1}{F_6 F_{2T} + F_{7T} F_1}, \\
\mathcal{L}_5(\mathbf{x}, t) &= \frac{\frac{\partial T_t}{\partial t} F_1 + \frac{\partial p_t}{\partial t} F_{2T} + \frac{\gamma p_t}{T_t} F_3 F_{2T} + \kappa F_3 F_1 - \mathcal{L}_1 (F_6 F_{2T} + F_{7T} F_1) - \mathcal{C}_{pt} F_{2T} - \mathcal{C}_{Tt} F_1}{F_4 F_{2T} + F_{5T} F_1}, \\
\mathcal{L}_2(\mathbf{x}, t) &= \frac{\frac{\partial T_t}{\partial t} + \kappa F_3 - \mathcal{L}_1 F_{7T} - \mathcal{L}_5 \cdot F_{5T} - \mathcal{C}_{Tt}}{F_{2T}}, \\
\mathcal{L}_3(\mathbf{x}, t) &= -\frac{\partial u_2}{\partial t} + \mathcal{C}_3, \\
\mathcal{L}_4(\mathbf{x}, t) &= -\frac{\partial u_3}{\partial t} + \mathcal{C}_4, \\
\mathcal{L}_6(\mathbf{x}, t) &= -\frac{\partial Y}{\partial t} + \mathcal{C}_6, \quad \mathbf{x} \in \Gamma_{in} \quad \text{with} \quad \kappa = \gamma - 1.
\end{aligned} \tag{3.56}$$

A linear relaxation is chosen by Odier [13],

$$\begin{aligned}
\frac{\partial p_t}{\partial t} + \eta_1 (p_t - p_{t,in}) &= 0, \\
\frac{\partial T_t}{\partial t} + \eta_2 (T_t - T_{t,in}) &= 0, \\
\frac{\partial u_2}{\partial t} + \eta_3 (u_2 - u_{2,in}) &= 0, \\
\frac{\partial u_3}{\partial t} + \eta_4 (u_3 - u_{3,in}) &= 0, \\
\frac{\partial Y}{\partial t} + \eta_6 (Y - Y_{in}) &= 0.
\end{aligned} \tag{3.57}$$

Here, the relaxation coefficients η_k are assumed to be constant. The CBC in Eq. (3.56) can be made partially reflecting by setting to zero the outgoing amplitude variation \mathcal{L}_1 or \mathcal{L}_5 . Further, the linear relaxation terms in Eq. (3.57) are inserted, and the term ζ in Eq. (3.45) is included to combine the formulations for $\Phi = 1$ and $\Phi = 5$,

$$\begin{aligned}\mathcal{L}_\Phi(\mathbf{x}, t) &= \frac{-\eta_2(T_t - T_{t,in})F_1 - \eta_1(p_t - p_{t,in})F_{2T} + \frac{\gamma p_t}{T_t}F_3F_{2T} + \kappa F_3F_1 - \mathcal{C}_{pt}F_{2T} - \mathcal{C}_{Tt}F_1}{0.5(1 - \zeta)(F_6F_{2T} + F_{7T}F_1) + 0.5(1 + \zeta)(F_4F_{2T} + F_{5T}F_1)}, \\ \mathcal{L}_2(\mathbf{x}, t) &= \frac{-\eta_2(T_t - T_{t,in}) + \kappa F_3 - 0.5(1 - \zeta)\mathcal{L}_1 \cdot F_{7T} - 0.5(1 + \zeta)\mathcal{L}_5F_{5T} - \mathcal{C}_{Tt}}{F_{2T}}, \\ \mathcal{L}_3(\mathbf{x}, t) &= \eta_3(u_2 - u_{2,in}) + \mathcal{C}_3, \\ \mathcal{L}_4(\mathbf{x}, t) &= \eta_4(u_3 - u_{3,in}) + \mathcal{C}_4, \\ \mathcal{L}_6(\mathbf{x}, t) &= \eta_6(Y - Y_{in}) + \mathcal{C}_6, \quad \mathbf{x} \in \Gamma_{in} \quad \text{with} \quad \kappa = \gamma - 1.\end{aligned}\tag{3.58}$$

Partially Non-Reflecting Inflow CBC Imposing Total Pressure, Static Temperature and Tangential Velocities

The wave amplitude variations, imposing the total pressure $p_{t,in}$, the static temperature T_{in} , as well as the to the boundary tangential velocities $u_{2,in}$ and $u_{3,in}$, can be derived analogue by exchanging the 3D-NSCBC expression for total temperature in equation system (3.54) with the expression for static temperature in Eq. (3.31),

$$\begin{cases} \mathcal{L}_5 \cdot F_4 - \mathcal{L}_2F_1 = \frac{\partial p_t}{\partial t} + \frac{\gamma p_t}{T_t}F_3 - \mathcal{L}_1 \cdot F_6 - \mathcal{C}_{pt}, \\ -\mathcal{L}_5F_5 + \mathcal{L}_2F_2 = \frac{\partial T}{\partial t} + \mathcal{L}_1F_5 - \mathcal{C}_T, \\ \frac{\partial u_2}{\partial t} = -\mathcal{L}_3 + \mathcal{C}_3, \\ \frac{\partial u_3}{\partial t} = -\mathcal{L}_4 + \mathcal{C}_4, \\ \frac{\partial Y}{\partial t} = -\mathcal{L}_6 + \mathcal{C}_6. \end{cases}\tag{3.59}$$

It is

$$\begin{aligned}F_1 &= \frac{e_c}{\rho T} \frac{\gamma p_t}{T_t}, \\ F_2 &= \frac{1}{\rho}, \\ F_3 &= u_2\mathcal{L}_3 + u_3\mathcal{L}_4, \\ F_4 &= \left(-\frac{1}{2} \frac{p_t}{p} + \frac{\gamma p_t}{T_t} \left(\frac{(\gamma - 1)e_c}{2\rho T} - \frac{u_1}{2\rho a} \right) \right), \\ F_5 &= \frac{\gamma - 1}{2\rho}, \\ F_6 &= \left(-\frac{1}{2} \frac{p_t}{p} + \frac{\gamma p_t}{T_t} \left(\frac{(\gamma - 1)e_c}{2\rho T} + \frac{u_1}{2\rho a} \right) \right).\end{aligned}\tag{3.60}$$

Solving for \mathcal{L}_k leads to

$$\begin{aligned}
\mathcal{L}_1(\mathbf{x}, t) &= \frac{\frac{\partial T}{\partial t} F_1 + \frac{\partial p_t}{\partial t} F_2 + \frac{\gamma p_t}{T_t} F_3 F_2 + \mathcal{L}_5 (F_4 F_2 - F_5 F_1) - \mathcal{C}_{pt} F_2 - \mathcal{C}_T F_1}{(F_5 F_1 - F_6 F_2)}, \\
\mathcal{L}_5(\mathbf{x}, t) &= \frac{\frac{\partial T}{\partial t} F_1 + \frac{\partial p_t}{\partial t} F_2 + \frac{\gamma p_t}{T_t} F_3 F_2 + \mathcal{L}_1 (F_5 F_1 - F_6 F_2) - \mathcal{C}_{pt} F_2 - \mathcal{C}_T F_1}{(F_4 F_2 - F_5 F_1)}, \\
\mathcal{L}_2(\mathbf{x}, t) &= \frac{\frac{\partial T}{\partial t} + \mathcal{L}_1 F_5 + \mathcal{L}_5 F_5 - \mathcal{C}_T}{F_2}, \\
\mathcal{L}_3(\mathbf{x}, t) &= -\frac{\partial u_2}{\partial t} + \mathcal{C}_3, \\
\mathcal{L}_4(\mathbf{x}, t) &= -\frac{\partial u_3}{\partial t} + \mathcal{C}_4, \\
\mathcal{L}_6(\mathbf{x}, t) &= -\frac{\partial Y}{\partial t} + \mathcal{C}_6, \quad \mathbf{x} \in \Gamma_{in}.
\end{aligned} \tag{3.61}$$

A linear relaxation is applied,

$$\begin{aligned}
\frac{\partial p_t}{\partial t} + \eta_1 (p_t - p_{t,in}) &= 0, \\
\frac{\partial T}{\partial t} + \eta_2 (T - T_{in}) &= 0, \\
\frac{\partial u_2}{\partial t} + \eta_3 (u_2 - u_{2,in}) &= 0, \\
\frac{\partial u_3}{\partial t} + \eta_4 (u_3 - u_{3,in}) &= 0, \\
\frac{\partial Y}{\partial t} + \eta_6 (Y - Y_{in}) &= 0.
\end{aligned} \tag{3.62}$$

The outgoing wave amplitudes are set to zero. Further, the relaxation terms in Eq. (3.62) and ζ in Eq. (3.45) are inserted into Eq. (3.59),

$$\begin{aligned}
\mathcal{L}_\Phi(\mathbf{x}, t) &= \frac{-\eta_2 (T - T_{in}) F_1 - \eta_1 (p_t - p_{t,in}) F_2 + \frac{\gamma p_t}{T_t} F_3 F_2 - \mathcal{C}_{pt} F_2 - \mathcal{C}_T F_1}{0.5 (1 - \zeta) (F_5 F_1 - F_6 F_2) + 0.5 (1 + \zeta) (F_4 F_2 - F_5 F_1)}, \\
\mathcal{L}_2(\mathbf{x}, t) &= \frac{-\eta_2 (T - T_{in}) + 0.5 (1 - \zeta) F_5 \mathcal{L}_1 + 0.5 (1 + \zeta) F_5 \mathcal{L}_5 - \mathcal{C}_T}{F_2}, \\
\mathcal{L}_3(\mathbf{x}, t) &= \eta_3 (u_2 - u_{2,in}) + \mathcal{C}_3, \\
\mathcal{L}_4(\mathbf{x}, t) &= \eta_4 (u_3 - u_{3,in}) + \mathcal{C}_4, \\
\mathcal{L}_6(\mathbf{x}, t) &= \eta_6 (Y - Y_{in}) + \mathcal{C}_6, \quad \mathbf{x} \in \Gamma_{in}.
\end{aligned} \tag{3.63}$$

3.5 Implementation

The application of CBC can be separated into four steps.

1. By calculation of the eigenvalues λ , the wave amplitude variations leaving the computational domain can be separated from those entering the domain. Details on this step can be found in chapter 3.2.
2. Calculation of the wave amplitude variations \mathcal{L}_k leaving the domain with Eq. (3.18).
3. In a third step, one has to close the chosen NSCBC system with meaningful boundary conditions. Details on this step are presented in chapter 3.4. Subsequently, one can calculate the wave amplitude variations which are entering the computational domain.
4. Finally, the right hand side is calculated using Eq. (3.26).

3.6 Injection of Turbulence

The injection of synthetic turbulence through a non-reflecting inflow boundary condition is difficult since both, turbulence fluctuations and the acoustic waves leaving the domain, produce velocity and pressure perturbations. A non-reflecting turbulence injection can be achieved by a low Mach number expansion and the separation of integral and acoustic length scales [17, 8]. By only considering the zeroth order terms, neglecting tangential terms and assuming that no acoustic pressure is produced, the inertial momentum equations used to inject turbulence can be derived as [8]

$$\frac{\partial u_1}{\partial t} + u_1 \frac{\partial u_1}{\partial x} = 0, \quad \frac{\partial p}{\partial t} = 0. \quad (3.64)$$

By inserting Eq. (3.64) into the wave amplitude variations in Eq. (3.28), and neglecting tangential and viscous terms the turbulent contribution is separated,

$$\begin{aligned} \mathcal{L}_1 &= - \left(\frac{\partial \overset{0}{p}}{\partial t} - \rho a \frac{\partial u_1}{\partial t} \right) \Rightarrow \mathcal{L}_1^i = \rho a \frac{\partial u_1'}{\partial t}, \\ \mathcal{L}_5 &= - \left(\frac{\partial \overset{0}{p}}{\partial t} + \rho a \frac{\partial u_1}{\partial t} \right) \Rightarrow \mathcal{L}_5^i = -\rho a \frac{\partial u_1'}{\partial t}, \\ \mathcal{L}_2^i &= 0, \quad \mathcal{L}_3^i = -\frac{\partial u_2'}{\partial t}, \quad \mathcal{L}_4^i = -\frac{\partial u_3'}{\partial t}. \end{aligned} \quad (3.65)$$

This formulation is called vortical-flow CBC [8]. The inertial contribution is added to the incoming amplitudes derived in chapter 3.4 in order to inject synthetic turbulence [13],

$$\begin{aligned}\mathcal{L}_1^{turb} &= \mathcal{L}_1 + \rho a \frac{\partial u'_1}{\partial t}, \\ \mathcal{L}_3^{turb} &= \mathcal{L}_3 - \frac{\partial u'_2}{\partial t}, \\ \mathcal{L}_4^{turb} &= \mathcal{L}_4 - \frac{\partial u'_3}{\partial t}, \\ \mathcal{L}_5^{turb} &= \mathcal{L}_5 - \rho a \frac{\partial u'_1}{\partial t}.\end{aligned}\tag{3.66}$$

In this thesis, the turbulence signal is generated using the approach by Batten et al. [1],

$$\begin{aligned}u'_k(x_j, t) &= a_{ki} \sqrt{\frac{2}{N_{rm}}} \sum_{n=1}^{N_{rm}} \left[p_i^n \cos(\hat{d}_j^n \hat{x}_j + \omega^n \hat{t}) + q_i^n \sin(\hat{d}_j^n \hat{x}_j + \omega^n \hat{t}) \right], \\ \text{with } \hat{x} &= \frac{2\pi x_j}{L_t}, \quad \hat{t} = \frac{2\pi t}{\tau_t}, \quad \hat{d}_j^n = d_j^n \frac{L_t}{c^n \tau_t}, \\ \text{and } c^n &= \sqrt{\frac{3(u_l u_m)_{in} d_l^n d_m^n}{2d_k^n d_k^n}}, \quad p_i^n = \epsilon_{ijk} \psi_j^n d_k^n, \quad q_i^n = \epsilon_{ijk} \xi_j^n d_k^n, \\ \psi_i^n, \xi_i^n &= N(0, 1), \quad \omega^n = N(1, 1), \quad d_i^n = N\left(0, \frac{1}{2}\right).\end{aligned}\tag{3.67}$$

The signal is generated by a sum of Fourier modes. The term a_{ki} is the Cholesky decomposition of the Reynolds stress tensor $(u_i u_j)_{in}$. The turbulent length scales and time scales are denoted L_t and τ_t . The number of Fourier modes is defined by N_{rm} . $N(\Phi, \Psi)$ is the normal distribution with a mean value Φ and a standard deviation Ψ , and ϵ_{ijk} is the permutation tensor. The scaling of the turbulence intensities is applied by c^n .

The generated turbulence field is considered as frozen turbulence field $\hat{t} = 0$, and convected with the mean velocity in flow direction, $\hat{x} = \frac{2\pi}{L_t}(x_1 - u_{1,in}t)$. Eq. (3.67) is derived in space as

$$\frac{\partial u'_k(x_j, t)}{\partial x} = a_{ki} \sqrt{\frac{2}{N}} \sum_{n=1}^N \hat{d}_1^n \frac{2\pi}{L} \left[p_i^n (-1) \sin(\hat{d}_j^n \hat{x}_j) + q_i^n \cos(\hat{d}_j^n \hat{x}_j) \right].\tag{3.68}$$

The time derivative is calculated from the derivative in space using Taylor's frozen turbulence hypothesis,

$$\frac{\partial u'_i}{\partial t} = -u_{1,in} \frac{\partial u'_i}{\partial x}.\tag{3.69}$$

Chapter 4

Validation of the Implemented Characteristic Boundary Conditions

4.1 Convergence in a Flow Channel with Periodic Boundaries

The following section aims at the evaluation of the attainment of the prescribed values for the inflow CBC in Eq. (3.63), as well as the outflow CBC in Eq. (3.53). Here, the inflow CBC imposes the total pressure, the static temperature and the tangential velocities, while the outflow CBC imposes the mean static pressure. The tangential terms \mathcal{T} and the viscous terms \mathcal{D} are set to zero for the inflow CBC.

Further, the pressure driven development of the flow field is investigated. In case the calculation is initialized with a quiescent flow field, the rate of convergence to the final Mach number can be slow depending on the chosen set of relaxation coefficients. For that reason three test cases are conducted using different combinations of relaxation coefficients η_k and σ^* .

Table 4.1: Parameters for the flow channel with periodic boundaries.

Test case	A1	A2	A3
Inflow BC	CBC Eq. (3.63): $p_{t,in}, T_{in}, u_{2,in}, u_{3,in}$		
Outflow BC	CBC Eq. (3.53): p_{out}		
Inflow relaxation	$\eta_k = 0.01$	$\eta_k = 0.1$	$\eta_k = 1.0$
Outflow relaxation	$\sigma^* = 0.25$	$\sigma^* = 5.0$	$\sigma^* = 2000.0$
Mach number	$M_\infty = 0.37$		
Ratio of specific heats	$\gamma = 1.4$		
Reynolds number	$Re = 100\,000$		

The specifications of the test cases can be found in Table 4.1. The computational domain and the positions of the boundary conditions are shown in Fig. 4.1. A uniformly refined,

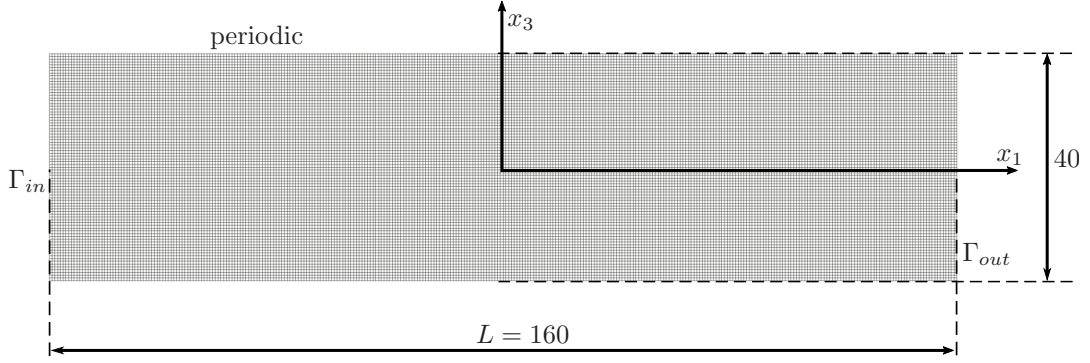


Figure 4.1: Slice of the computational domain of the flow channel at $x_2 = 0$.

3D-rectangular box with the dimensions $[160, 40, 40]$ and 2 048 000 cells is simulated. The boundary conditions in x_2 - and x_3 -directions are periodic.

The quiescent flow field is initialized as

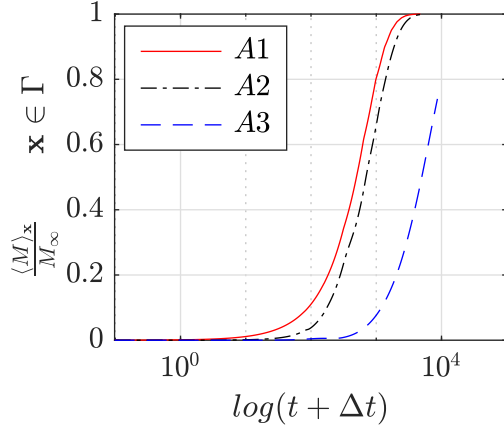
$$\rho_0 = T_0^{\frac{1}{\gamma-1}}, \quad \mathbf{u}_0 = 0, \quad p_0 = \frac{\rho_0 T_0}{\gamma}, \quad \text{and} \quad T_0 = 1. \quad (4.1)$$

The target values are calculated using the isentropic relations,

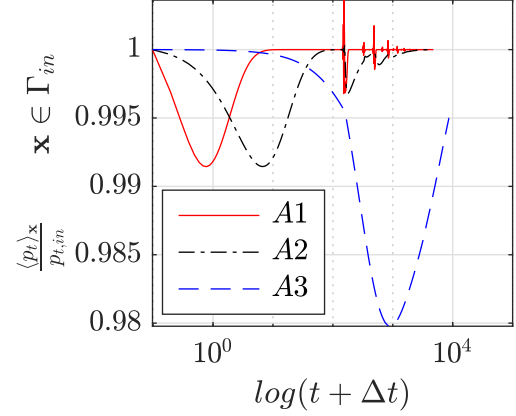
$$\begin{aligned} p_{t,in} &= \gamma^{-1}, \\ T_{in} &= \left(1 + \frac{1}{2} (\gamma - 1) M_\infty^2 \right)^{-1}, \\ u_{2,in} &= 0, \quad u_{3,in} = 0, \\ p_{out} &= \frac{1}{\gamma} \left(1 + \frac{1}{2} (\gamma - 1) M_\infty^2 \right)^{-\left(\frac{\gamma}{\gamma-1}\right)}, \end{aligned} \quad (4.2)$$

with the prescribed Mach number $M_\infty = 0.37$. Because of the ratio of total pressure at the inflow and static pressure at the outflow, the flow converges towards M_∞ . A Reynolds number of $Re = 10^5$ and an isentropic exponent of $\gamma = 1.4$ are used for all three test cases.

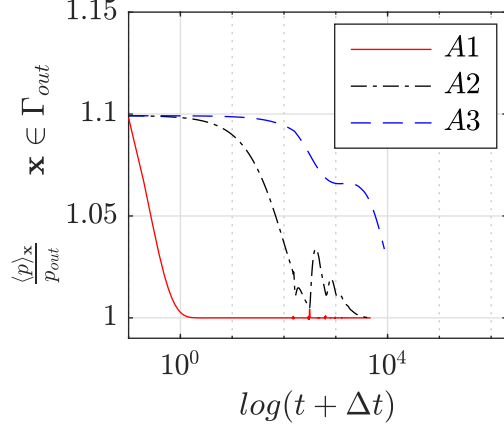
Fig. 4.2a shows the temporal development of the Mach number averaged over all cells of the domain Γ and normalized with its target value M_∞ . The averaging operator in space is denoted as $\langle \cdot \rangle_{\mathbf{x}}$. In Fig. 4.2b, 4.2c and 4.2d, the temporal development of total pressure p_t and static temperature T at the inflow, and the static pressure p at the outflow boundary are plotted. Here, the values are spatially averaged over all corresponding characteristic boundary cells of inflow Γ_{in} and outflow Γ_{out} . All values are normalized with the prescribed values $p_{t,in}$, T_{in} and p_{out} . The time t is plotted in a logarithmic scale. Since $\log(t = 0)$ is undefined, the time t is incremented by the time step Δt , in order to visualize the quiescent flow field at $t = 0$.



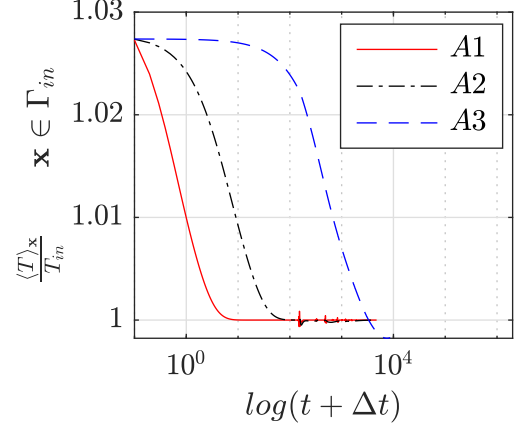
(a) Convergence of the Mach number $\langle M \rangle_{\mathbf{x}}$ averaged over all cells of the domain Γ and normalized with the prescribed Mach number M_{∞} .



(b) Convergence of the total pressure $\langle p_t \rangle_{\mathbf{x}}$ averaged over the cells of the inflow boundary Γ_{in} and normalized with the target total pressure $p_{t,in}$.



(c) Convergence of the static pressure $\langle p \rangle_{\mathbf{x}}$ averaged over the cells of the outflow boundary Γ_{out} and normalized with the target static pressure p_{out} .



(d) Convergence of the static temperature $\langle T \rangle_{\mathbf{x}}$ averaged over the cells of the inflow boundary Γ_{in} and normalized with the target static temperature T_{in} .

Figure 4.2: Convergence of the Mach number and the at the CBC imposed values.

The rate of convergence strongly depends on the relaxation coefficients η_k and σ^* as evident in Fig. 4.2a. Here, convergence is reached when the curve remains constant at $\frac{\langle M \rangle_x}{M_\infty} = 1$. The fastest convergence of the flow field can be observed for test case A1 where high relaxation coefficients are used. Test case A3 is canceled before reaching the state of convergence due to the slow rate of convergence. In Fig. 4.2b and 4.2d, the attainment of the prescribed values at the inflow boundary is shown. Both, the prescribed total pressure and the static temperature, reach and attain their prescribed values for the test cases A1 and A2. The same result can be observed in Fig. 4.2c for the prescribed static pressure at the outflow boundary. It might be recommended to start the calculation with higher values for the relaxation coefficients, and reduce the coefficients after the final Mach number is reached, even though this implies that the non-reflective behavior is dispensed for the initial ramp up phase.

4.2 Turbulence Injection into a Flow Channel

A turbulent signal is generated and injected into the flow channel shown in section 4.1. At the inflow, total pressure, static temperature and tangential velocities are imposed using the CBC in Eq. (3.63). The tangential terms \mathcal{T} and viscous terms \mathcal{D} are set to zero for the inflow CBC. At the outflow, a mean static pressure is imposed by the CBC in Eq. (3.53). The prescribed values are calculated using Eq. (4.2) with $M_\infty = 0.37$. The boundary conditions in x_2 - and x_3 -directions are periodic. The test case parameters are summarized in Table 4.2. The turbulent signal is generated by the approach of Batten et al. [1] described in Eq. (3.68) with the parameters in Table 4.2 and injected using Eq. (3.66). High values of η_k damp the injected turbulence. This effect becomes stronger with greater turbulence intensity [13]. Further, the imposed inflow variables can drift for low relaxation coefficients. The inflow relaxation coefficients η_k are chosen to be as small as possible in order to prevent damping as well as drifting.

The test case is compared to a reference case with the Neumann and Dirichlet type boundary conditions in Eq. (2.13) and (2.14) imposing

$$\begin{aligned} T_{in} &= \left(1 + \frac{1}{2} (\gamma - 1) M_\infty^2 \right)^{-1}, \\ \rho_{in} &= T_{in}^{\frac{1}{\gamma-1}}, \\ u_{1,in} &= M_\infty \sqrt{T_{in}}, \\ p_{out} &= \frac{1}{\gamma} \left(1 + \frac{1}{2} (\gamma - 1) M_\infty^2 \right)^{-\left(\frac{\gamma}{\gamma-1}\right)} \end{aligned} \quad (4.3)$$

using the same Mach number $M_\infty = 0.37$. For the reference case, the turbulent signal is generated by the same approach using Eq. (3.67) with the same parameters for the generated

turbulence. The turbulent fluctuations are added to the imposed mean velocity using Eq. (2.17).

Table 4.2: Parameters for the injection of turbulence.

Test case	B1	B2
Inflow BC	BC eq. (2.13): $\rho_{in}, \mathbf{u}_{in}$	CBC Eq. (3.63): $p_{t,in}, T_{in}, u_{2,in}, u_{3,in}$
Outflow BC	BC Eq. (2.14): p_{out}	CBC Eq. (3.53): p_{out}
Inflow relaxation	-	$\eta_k = 0.02$
Outflow relaxation	-	$\sigma^* = 0.25$
Mach number	$M_\infty = 0.37$	
Ratio of specific heats	$\gamma = 1.4$	
Reynolds number	$Re = 100\,000$	
Number of random modes:	$N_{rm} = 60$	
Turbulent length scale	$L_t = 24.0$	
Turbulent time scale	$\tau_t = \frac{L_t}{u_{1,in}}$	
Reynolds stresses	$(u'_i u'_i)_{in} = 0.0003331282$ $(u'_i u'_j)_{in} = 0.0$	

The turbulent kinetic energy is calculated as

$$TKE = \frac{1}{2} \left(\sum_i^3 u'_i u'_i \right). \quad (4.4)$$

Both, the turbulent kinetic energy and the Reynolds stresses $\rho u'_i u'_i$, are averaged in time $\langle \cdot \rangle_t$ and over the x_2 - x_3 -planes $\langle \cdot \rangle_{x_2, x_3}$, and plotted along the x_1 -direction in order to evaluate the generated turbulence.

The injection of the fluctuations in flow direction does not reach the values of the generated turbulence field as shown in Fig. 4.3a. In Fig. 4.3b and 4.3c, it can be observed that the tangential Reynolds stresses near the inflow boundary for the test case B2 are comparable to the reference case where the Neumann and Dirichlet type boundary conditions are used. With increasing distance to the inflow boundary, the tangential Reynolds stresses drop below the reference case B1. The Reynolds stresses result in a lower turbulent kinetic energy compared to test case B1 as shown in Fig. 4.4.

Summarized, the injected turbulence does not represent the calculated turbulent signal for the chosen implementation.

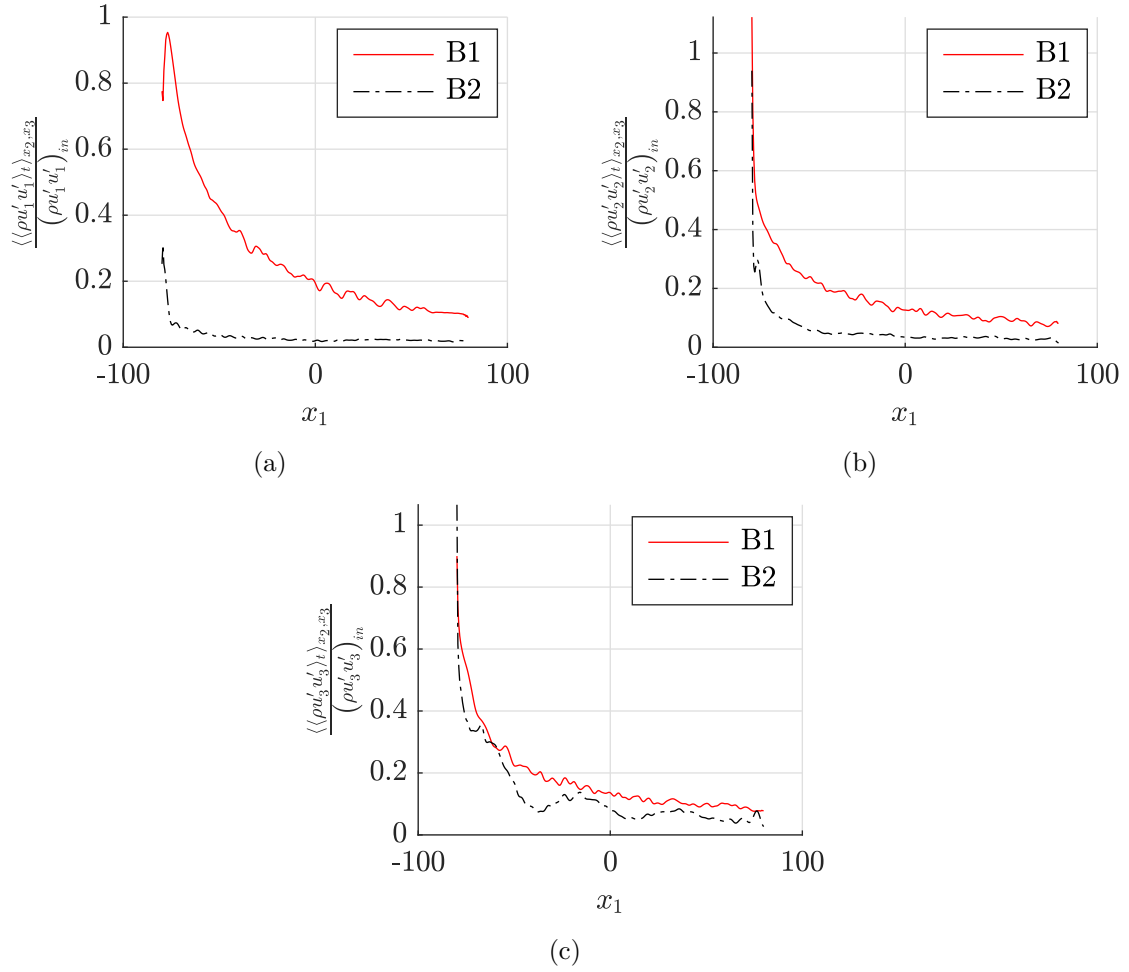


Figure 4.3: Reynolds stresses $\langle \rho u'_i u'_i \rangle_t \rangle_{x_2 x_3}$ spatially averaged over the x_2 - x_3 -planes, temporally averaged and normalized with the injected mean Reynolds stresses $(\rho u'_i u'_i)_{in}$.

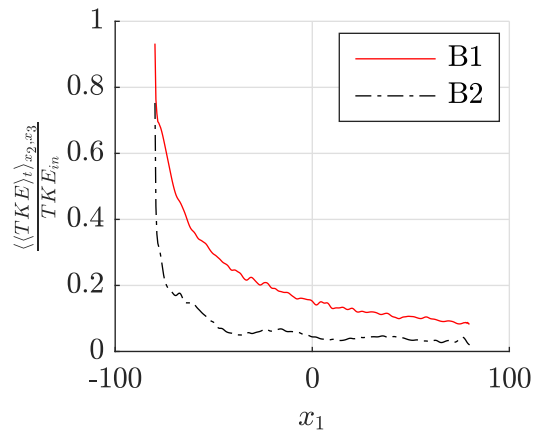


Figure 4.4: Turbulent kinetic energy $\langle \langle TKE \rangle_t \rangle_{x_2 x_3}$ spatially averaged over the x_2 - x_3 -planes, temporally averaged and normalized with the injected mean turbulent kinetic energy $(TKE)_{in}$.

4.3 Ability of the Outflow CBC to Represent a Rotational Flow

In this section, the capability of the outflow CBC in Eq. (3.53) to represent the pressure equilibrium that is usually found in the outflow of a turbomachinery flow is verified. The outflow CBC imposes mean static pressure. A test case is adapted from the work of Koupper et al. [9] simulating a free vortex flow inside an annulus geometry. The angular velocity of a free vortex rotating around the x_1 axis is calculated by

$$u_\phi = c_1/r, \quad r = \sqrt{x_2^2 + x_3^2}. \quad (4.5)$$

Here, $c_1 = 2$ is a constant value specifying the vorticity strength, and r is the radial coordinate. A specific pressure distribution arises due to the free vortex, that can be described by the analytical function [9],

$$p_{se}(r) = \alpha_{se} \exp\left(-\frac{\gamma c_1^2}{2Tr^2}\right), \quad (4.6)$$

$$\alpha_{se} = \frac{p_{out}(r_+^2 - r_-^2)}{\left[\left(c_1^2/(2\gamma^{-1}T)\right) Ei\left(-c_1^2/(2\gamma^{-1}Tr^2) + r^2 \exp\left(-c_1^2/(2\gamma^{-1}Tr^2)\right)\right)\right]_{r_-}^{r_+}}.$$

The analytical pressure distribution is derived from the simplified radial equilibrium equations [20]. The exponential integral function is defined as $Ei(x) = \int_{-\infty}^x \exp(t)/t dt$, and the closed interval is calculated as $[f(r)]_a^b = f(b) - f(a)$. The pressure p_{out} is the average of the analytical function p_{se} between r_- and r_+ .

The computational domain is shown in Fig. 4.5. The grid has 661.368 cells. The inner radius of the annulus is $r_- = 10$, the outer radius is $r_+ = 20$ and the length in x_1 -direction is $l = 50$. At the inflow CBC, the velocity and the static temperature are imposed using Eq. (3.48). Here, the tangential velocity components impose the free vortex. At the inner and outer annulus cylinder surfaces, the slip wall boundary condition in Eq. (2.16) is used. The initial condition and the imposed values are calculated as

$$T_{in} = T_0 = \left(1 + \frac{1}{2}(\gamma - 1) M_\infty^2\right)^{-1}, \quad \rho_0 = T_0^{\frac{1}{\gamma-1}},$$

$$u_{1,in} = u_{1,0} = M_\infty \sqrt{T_{in}},$$

$$u_{2,in} = u_{2,0} = u_\phi \cos \phi,$$

$$u_{3,in} = u_{3,0} = -u_\phi \sin \phi,$$

$$p_{out} = \frac{1}{\gamma} \left(1 + \frac{1}{2}(\gamma - 1) M_\infty^2\right)^{-\left(\frac{\gamma}{\gamma-1}\right)} \quad (4.7)$$

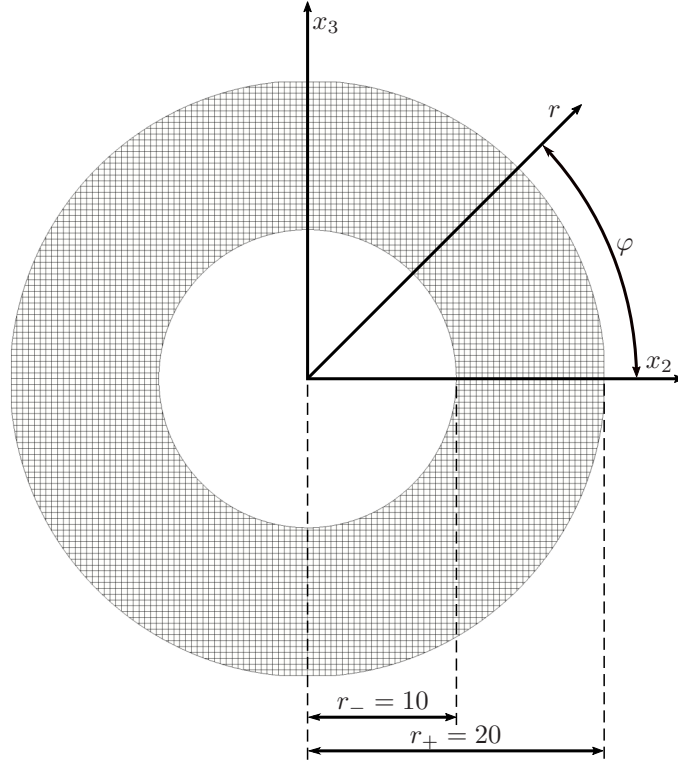


Figure 4.5: Slice of the computational domain of the annulus geometry at $x_1 = 0$.

using the Mach number $M_\infty = 0.37$. The Reynolds number is $Re = 10^5$, and the isentropic exponent is $\gamma = 1.4$.

The analytical solution is compared to the simulation data where the characteristic outflow boundary equations are solved. Since the pressure distribution at the outflow boundary with the patch averaged formalism is not fixed, the pressure curve should approach the analytical solution. Fig. 4.6 shows the simulation data at the outflow boundary at the coordinate $x_1 = 25$ along the analytical solution calculated with Eq. (4.6). The cell values for the pressure p of all boundary cells are fitted through a polynomial of third order. The analytical solution in Eq. (4.6) is shown with an error margin of $\pm 0.5\%$. One can see, that the simulation data lays inside or near the margin patch depending on the relaxation coefficient σ^* . For higher values of σ^* , the error between outflow pressure and the prescribed target value p_{out} becomes smaller.

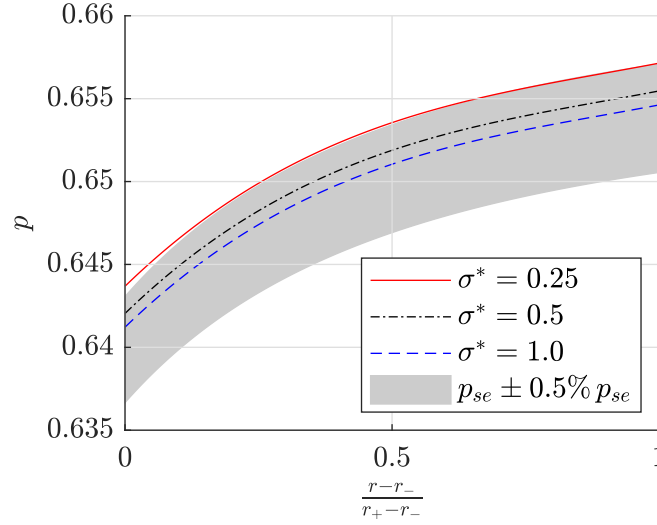


Figure 4.6: Pressure equilibrium at the outflow boundary for different relaxation coefficients σ^* compared to the analytical solution.

4.4 Permeability of the Characteristic Outflow Boundary Condition for a Vortex

The permeability of the outflow boundary condition for a vortex is tested. Here, the outflow CBC in Eq. (3.53) imposes a mean static pressure. The analytical solution of the vortex flow is [17]

$$\begin{aligned}
 \rho(x_1, x_2, t) &= \rho_{in} \cdot \exp\left(-\frac{1}{2} \left(\frac{c_2^2}{ar_v} \exp\left(-\frac{r^2}{r_v^2}\right)\right)\right), \\
 u_1(x_1, x_2, t) &= -\frac{c_2 x_2}{r_v^2} \exp\left(-\frac{r^2}{2r_v^2}\right) + u_{1,in}, \\
 u_2(x_1, x_2, t) &= \frac{c_2 (x_1 - u_{1,in}t)}{r_v^2} \exp\left(-\frac{r^2}{2r_v^2}\right), \\
 u_3 &= 0, \\
 p(x_1, x_2, t) &= p_{out} \cdot \exp\left(-\frac{1}{2} \left(\frac{c_2^2}{ar_v} \exp\left(-\frac{r^2}{r_v^2}\right)\right)\right).
 \end{aligned} \tag{4.8}$$

The characteristic size of the vortex is defined as $r_v = 5$, and the vortex strength is $c_2 = 2$. The vortex is transported through the velocity $u_{1,in}$ in x_1 -direction. The radial coordinate r lays inside the vortex such that

$$r = \sqrt{(x_1 - u_{1,in}t)^2 + x_2^2}. \tag{4.9}$$

The computational domain of the size $[40, 250, 40]$ has 522 512 cells. Here, the inner volume of the domain at $20 < x_2 < 20$ is finer resolved with 314 432 cells. At the inflow, the CBC in Eq. (3.63) is used imposing total pressure, static temperature and tangential velocities. The tangential terms \mathcal{T} and the viscous terms \mathcal{D} are set to zero for the inflow CBC. For the

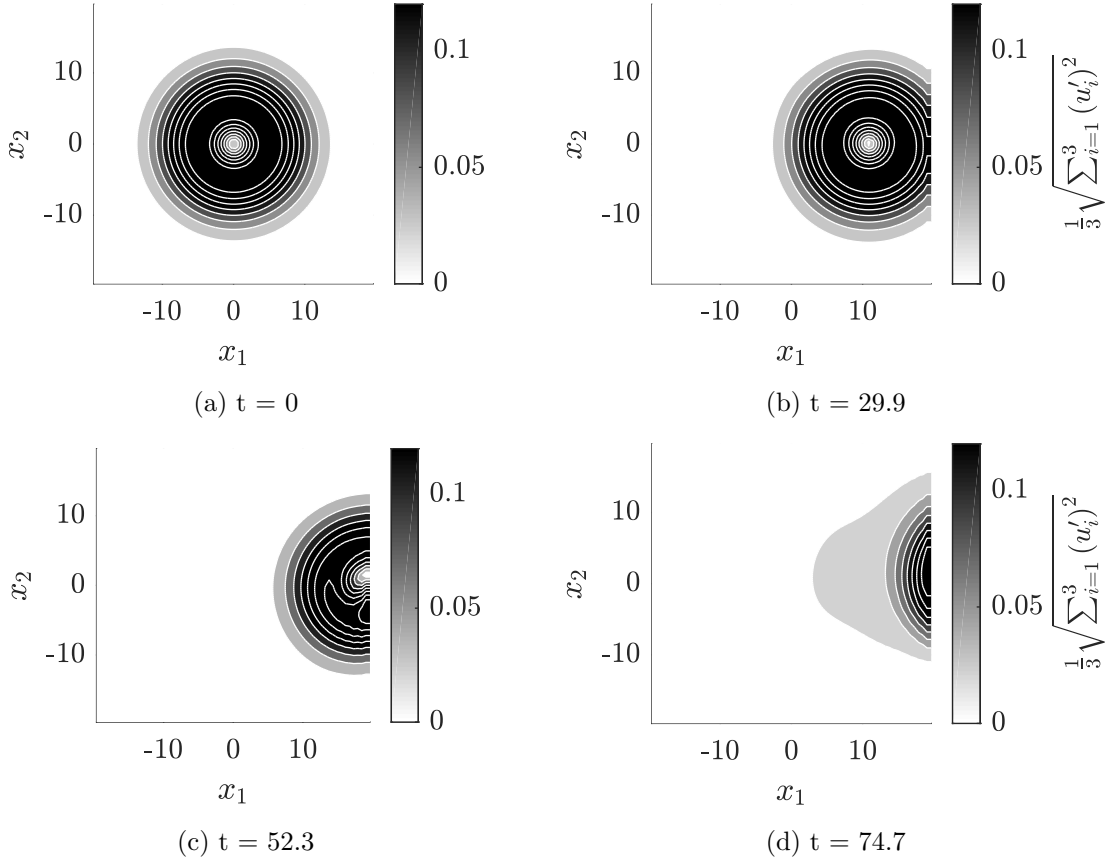


Figure 4.7: Vortex leaving the computational domain through the Neumann and Dirichlet type boundary condition in Eq. (2.14). Slice at $x_3 = 0$.

outflow CBC a relaxation coefficient of $\sigma^* = 0.25$ is used. The boundary conditions in x_2 - and x_3 -directions are periodic. The initial condition is calculated from the analytical solution in Eq. (4.8) at the time $t = 0$ leading to the initial vortex position $x_1 = 0$ and $x_2 = 0$. The prescribed values at the boundaries and in the analytical solution are calculated from Eq. (4.2) and (4.3) with $M_\infty = 0.37$.

For comparison, the same test case is conducted with Neumann and Dirichlet type boundary Eq. (2.13) imposing the velocities and the density, and Eq. (2.14) imposing the static pressure. The target values are calculated from Eq. (4.3) with $M_\infty = 0.37$. A sponge layer damping pressure waves is placed at the outflow for $x_1 > 19$ using a sponge factor of 5.0.

In Fig. 4.7 and 4.8, it is shown how the vortices are crossing the boundary. In Fig. 4.7, the Neumann and Dirichlet type boundary conditions are used. The structure of the vortex is visibly affected by crossing the outflow. In the test case using the CBC in Fig. 4.8, the vortex is not affected and the structure stays intact.

The test case is repeated for multiple values of the relaxation coefficient σ^* . In Fig. 4.9, the pressure fluctuations and the total velocity fluctuations are plotted for all test cases along the line $x_2 = 0$ and $x_3 = 0$. Further, the pressure p_{out} and the velocity $u_{1,in}$ are subtracted

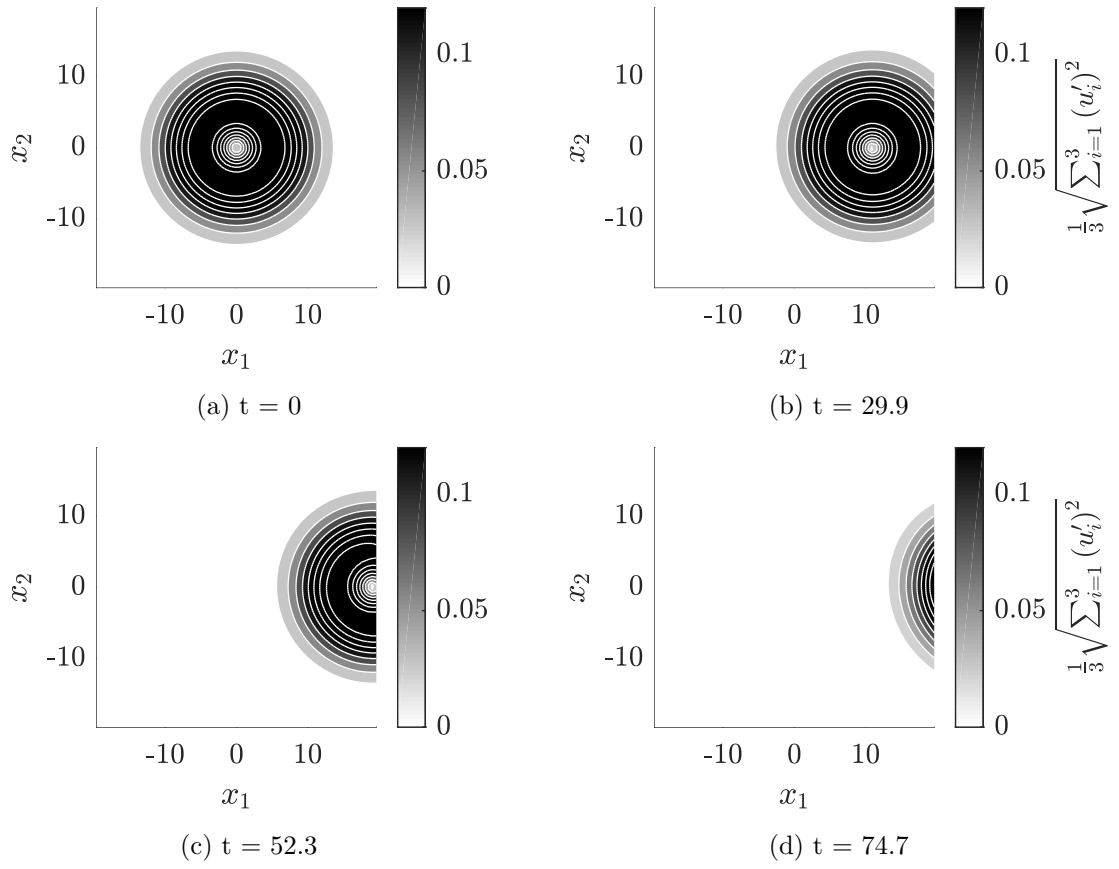
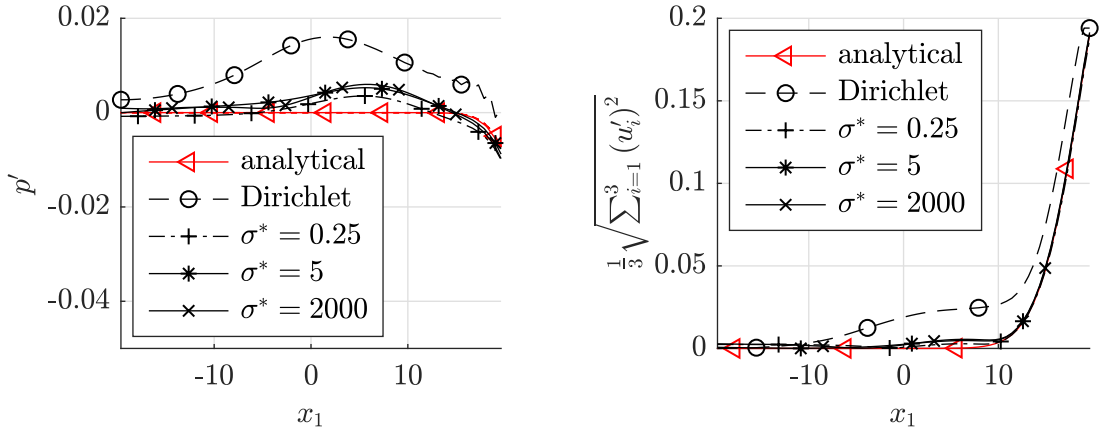


Figure 4.8: Vortex leaving the computational domain through the CBC in Eq. (3.53). Relaxation coefficient $\sigma^* = 0.25$. Slice at $x_3 = 0$.



(a) Pressure fluctuations due to the vortex. (b) Total velocity fluctuations due to the vortex.
Figure 4.9: Pressure and total velocity fluctuations at the line $x_2 = 0$ and $x_3 = 0$. Time $t = 74.7$.

from the analytical solution in Eq. (4.8), and the analytical solution is plotted.

The differences between the analytical solution and the simulation data in Fig. 4.9a is due to pressure waves arising from the vortex crossing the outflow domain. The pressure waves, in case of the CBC, are lower compared to the Neumann and Dirichlet type boundary condition. Only a small increase of the amplitude can be observed for high values of the relaxation coefficient σ^* . A high consistency between analytical solution and simulation data for the velocity fluctuation is shown in Fig. 4.9b for all relaxation coefficients σ^* using the CBC. The Neumann and Dirichlet type boundary conditions show a high difference in the total velocity fluctuation compared to the analytical solution.

4.5 Reflectivity of the Characteristic Inflow and Outflow Boundary Conditions for Acoustic Waves

The inflow CBC in Eq. (3.63), imposing total pressure and static temperature, has the ability to remain partial non-reflective while turbulence is injected. This is verified in this section by evaluating the reflections of acoustic waves. Further, it is shown that the outflow CBC in Eq. (3.53), imposing mean static pressure, is partial non-reflective while the injected turbulence and an acoustic wave are leaving the domain through the outflow.

The same computational domain as in the sections 4.1 and 4.2 is used illustrated in Fig. 4.1. The tangential terms \mathcal{T} and the viscous terms \mathcal{D} are set to zero for the inflow CBC. The boundary conditions in x_2 - and x_3 -directions are periodic. The prescribed values are calculated using Eq. (4.2) with $M_\infty = 0.37$. The same turbulent signal as in section 4.2 is injected generated by Eq. (3.68), and injected using Eq. (3.66). The properties of the

turbulence are given by Table 4.2.

As comparison, a reference case is calculated using the inflow boundary condition in Eq. (2.13), imposing velocity and density. At the outflow, the boundary condition in Eq. (2.14), imposing static pressure, is used. For this test case, the turbulence is generated using the same approach in Eq. (3.67), and added to the mean velocity as in Eq. (2.17).

A pressure pulse,

$$p' = 0.05, \quad x \in \{-5 \leq x \leq 5\}, \quad (4.10)$$

is added to the converged solutions. Two acoustic waves arise from this pressure pulse, traveling with a speed $u-a$ and $u+a$ in negative and positive x_1 -direction with a pressure amplitude of approximately $p_{ac} = 0.278$. After the waves reach the inflow and outflow boundaries their reflections can be evaluated. The test case is repeated for different relaxation coefficients η_k and σ^* , as well as for the reference case. The parameters of the different test cases are summarized in Table 4.3.

In Fig. 4.10a to 4.10c, the traversal of the acoustic waves can be observed for test case E3. The reflections of this test case are shown in Fig. 4.10d. The reflections for all test cases are plotted in Fig. 4.11 normalized with the pressure amplitude p_{ac} . Here, reflections of the inflow boundary can be found at $x_1 < 0$, while the reflections of the outflow boundary are located at $x_1 > 0$.

The outflow CBC does not reflect the acoustic wave for low values of the relaxation coefficients σ^* , while the Neumann and Dirichlet type BC produces a reflection of the acoustic wave of nearly the same amplitude. The reflection of the inflow CBC in test case E3 has an pressure amplitude of approximately $0.2p_{ac}$, while the amplitude of the reflection using the Neumann and Dirichlet type BC in test case E1 is nearly $0.7p_{ac}$. Using a zero relaxation coefficient η_k leads to no reflections at the inflow, but this case is not stable with the combined turbulence injection. Increasing the relaxation coefficient at the characteristic inflow and outflow boundary condition leads to significantly higher reflected pressure amplitudes.

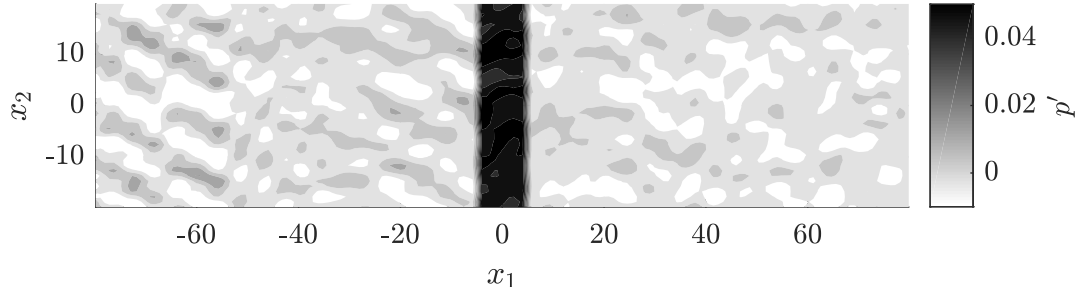
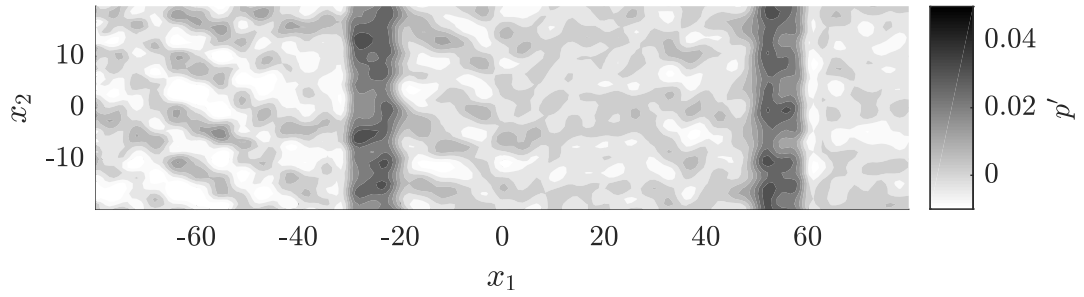
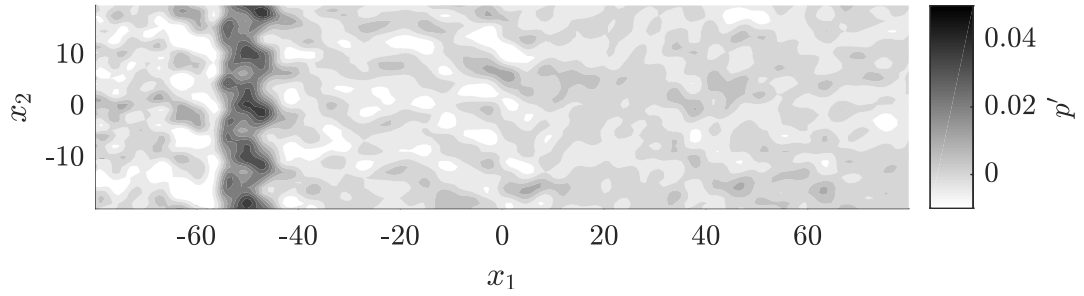
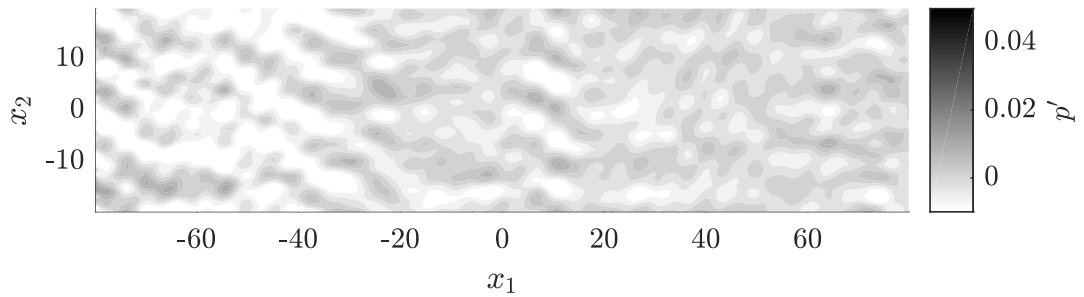
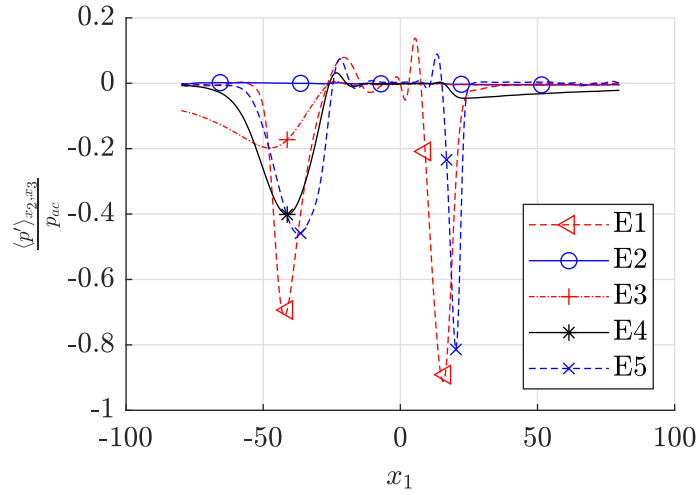
(a) $t = 0$.(b) $t = 39.06$.(c) $t = 78.13$.(d) $t = 156.25$.

Figure 4.10: Test case E3: $\eta_k = 0.02$, $\sigma^* = 0.25$. Injected pressure waves leaving the computational domain. Reflections of those pressure waves can be observed in Fig. 4.10d.

Table 4.3: Parameters for the evaluation of the reflections of acoustic waves.

Test case	E1	E2	E3	E4	E5
Inflow BC	BC Eq. (2.13): $\rho_{in}, \mathbf{u}_{in}$		CBC Eq. (3.63): $p_{t,in}, T_{in}, u_{2,in}, u_{3,in}$		
Outflow BC	BC Eq. (2.14): p_{out}		CBC Eq. (3.53): p_{out}		
Inflow relaxation	-	$\eta_k = 0$	$\eta_k = 0.02$	$\eta_k = 0.1$	$\eta_k = 1.0$
Outflow relaxation	-	$\sigma^* = 0.25$	$\sigma^* = 0.25$	$\sigma^* = 5.0$	$\sigma^* = 2000.0$
Mach number	$M_\infty = 0.37$				
Ratio of specific heats	$\gamma = 1.4$				
Reynolds number	$Re = 100\,000$				

Figure 4.11: Reflections of the injected acoustic waves at $t = 156.25$ spatially averaged over the x_2 - x_3 -planes.

Chapter 5

Application in a Turbine-Like Setup

In the following, the presented CBC are compared with Neumann and Dirichlet type boundary conditions in a turbine-like setup. A representation of the computational domain, used in all calculations, is illustrated in Fig. 5.1. The simplified turbine geometry resembles a turbine with infinite hub radius, so that the x_3 -direction can be interpreted as radial coordinate. The tapering in negative x_3 -direction, the angle of the segment and the turbine blading are neglected in favor of simplification. The domain includes the main annulus flow and the wheel space flow. Cooling gas is introduced into the wheel space to prevent the main flow from entering the wheel space. The main flow of the turbine is located at $116 < x_3 < 160$. The wheel space cavity, where the cooling gas enters the main flow, is located at the hub wall of the turbine in the area $-2 < x_1 < 2$ and $x_3 = 116$. A width of $\Delta x_2 = 32$ is chosen for the main flow and a major part of the wheel space. The values imposed at the wheel space inflow lead to a mass flow rate multiple orders smaller than the mass flow rate through the main annulus. Since the specification of extremely small velocities at the inflow boundaries can be numerical challenging, the width of the wheel space inflow is reduced to a value of $\Delta x_2 = 10$ to be able to increase the inflow velocity, while the average mass flow rate through the wheel space can remain constant.

The inflow boundary of the main annulus Γ_{in}^{mf} is located in negative x_1 -direction, while the outflow boundary Γ_{in}^{mf} is located in positive x_1 -direction. The inflow boundary of the wheel space Γ_{in}^{wsf} can be found in negative x_1 -direction below $x_3 < 71$. Periodic boundary conditions are applied in x_2 -direction where the width of the domain is $\Delta x_2 = 32$. The outer wall of the main annulus is modeled using the slip boundary condition in Eq. (2.16), while the inner wall of the main annulus, as well as the walls of the wheel space are modeled by the wall boundary condition in Eq. (2.15). A wall velocity of $u_{2,w} = 0.68493 \cdot u_{1,in} \cdot \frac{x_3}{116}$ is imposed at $x_1 \geq 2$ and $x_3 > 73$. Otherwise a zero wall velocity is imposed.

The grid has a resolution of 6 103 392 cells and three levels of refinement. The cell widths are $\Delta x = [0.122, 0.244, 0.488]$. The inner volume of the main annulus exhibits the lowest resolution and the wheel space the medium resolution. Main inflow and outflow boundaries, as well as the inner wall of the main annulus and the wheel space cavity region are refined at the highest resolution.

Three different test cases are calculated where the inflow and outflow boundary conditions vary. A summary of the test cases is given in Table 5.1. For the test case F1, the Neumann and Dirichlet type boundary conditions in Eq. (2.13) and Eq. (2.14) are applied at the main annulus inflow and outflow, as well as the wheel space inflow. Here, the inflow boundary condition imposes the density and the velocity, while the outflow boundary condition imposes the static pressure. In test case F2 the total pressure, the static temperature and the tangential velocities are imposed at the inflow boundaries of main annulus and wheel space using the CBC in Eq. (3.63), while the mean static pressure is imposed at the main annulus outflow by the CBC in Eq. (3.53). Test case F3 is identical to case F2, except that the velocity in x_1 -direction is imposed at the wheel space inflow instead of the total pressure. This is done by applying the CBC in Eq. (3.48). For the inflow boundary condition, imposing the total pressure, the tangential terms \mathcal{T} and viscous terms \mathcal{D} are set to zero. The imposed values for the boundary conditions are calculated using Eq. (4.2) and Eq. (4.3) with different Mach numbers for main annulus flow and wheel space flow. The main flow Mach number is $M_\infty^{mf} = 0.37$, and the wheel space flow Mach number is $M_\infty^{wsf} = 0.0005$ for all test cases. At the inflow boundaries of test case F1 a density sponge up to $x_1 = -59$ and a sponge factor of 5.0 is used. Further, a pressure sponge is used at the outflow at $x_1 > 29$ with the same sponge factor. The flow field is initialized as a quiescent flow using Eq. (4.1) and $M_\infty^{mf} = 0.37$.

The calculations, using the CBC, can be divided into three phases in regard to time. In the initial phase the velocity of the main annulus is ramped up. In the second phase, the relaxation coefficients of the CBC are lowered in order to achieve partially non-reflecting boundary conditions. The relaxation coefficients $\eta_k \approx 40$ and $\sigma^* = 2200$ are used for wheel space and main flow of test case F2 without reducing the values, since the test case was canceled before initializing the second phase. This is because it showed to be complicated, controlling the mass flow rate inside the wheel space by imposing a total pressure at the wheel space inflow. For test case F3 the coefficients are lowered at $t/t_{ref} = 16.68$ from $\eta_k = 1.0$ and $\sigma^* = 2000$ to $\eta_k = 0.5$ and $\sigma^* = 0.25$. The time t is normalized using the approximate traversal time $t_{ref} = L^{mf}/u_{1,in}^{mf} = 246.58$ from main inflow to outflow. Relatively high values of the inflow relaxation coefficients η_k are chosen at the main flow CBC (3.63) compared to the test case in section 4.2. These high values showed to be necessary for this test case, since

low values led to instabilities at the inflow plane. It is not clear where the limit to instability lies. At the wheel space inflow of test case F3, constant values of $\eta_k^* = \pm 0.278$ are used in all phases. Turbulence is injected in the final phase at $t/t_{ref} > 71.1$. In test case F1 the first and second phase are identical since no relaxation is applied to the Neumann and Dirichlet type boundary conditions. After $t/t_{ref} > 71.25$, the third phase begins for test case F1, and turbulence is imposed at the main annulus inflow.

The synthetic turbulence is calculated by the approach of Batten et al. [1] for both test cases F1 and F3, using the coefficients in Table 5.1. For test case F1 the turbulent signal is calculated by Eq. (3.67) and imposed using Eq. (2.17), while for test case F3 the turbulent signal is calculated using Eq. (3.68) and injected by Eq. (3.66).

Table 5.1: Setups of the turbine-like application.

Test case	F1	F2	F3
Main annulus inflow	BC Eq. (2.13): $\rho_{in}, \mathbf{u}_{in}$	CBC Eq. (3.63): $p_{t,in}, T_{in}, u_{2,in}, u_{3,in}$	
Main annulus outflow	BC Eq. (2.14): p_{out}	CBC Eq. (3.53): p_{out}	
Wheel space inflow	BC Eq. (2.13): $\rho_{in}, \mathbf{u}_{in}$	CBC Eq. (3.63): $p_{t,in}, T_{in}, u_{2,in}, u_{3,in}$	CBC Eq. (3.48): T_{in}, \mathbf{u}_{in}
Mach number	$M_\infty^{mf} = 0.37$		
Ratio of specific heats	$\gamma = 1.4$		
Reynolds number	$Re = 100\,000$		
Main inflow relaxation	-	$\eta_k \approx 40$	$t/t_{ref} < 16.68$: $\eta_k = 1.0$ $t/t_{ref} \geq 16.68$: $\eta_k = 0.5$
Wheel space inflow relaxation	-	$\eta_k \approx 40$	$\eta_k^* = \pm 0.278$
Main outflow relaxation	-	$\sigma^* = 2200$	$t/t_{ref} < 16.68$: $\sigma^* = 2000$ $t/t_{ref} \geq 16.68$: $\sigma^* = 0.25$
Turbulence injection	$t/t_{ref} \geq 71.25$	-	$t/t_{ref} \geq 71.1$
Number of random modes:		$N_{rm} = 60$	
Turbulent length scale		$L_t = 24.0$	
Turbulent time scale		$\tau_t = \frac{L_t}{u_{1,in}}$	
Reynolds stresses		$(u'_i u'_i)_{in} = 0.0003331282$ $(u'_i u'_j)_{in} = 0.0$	

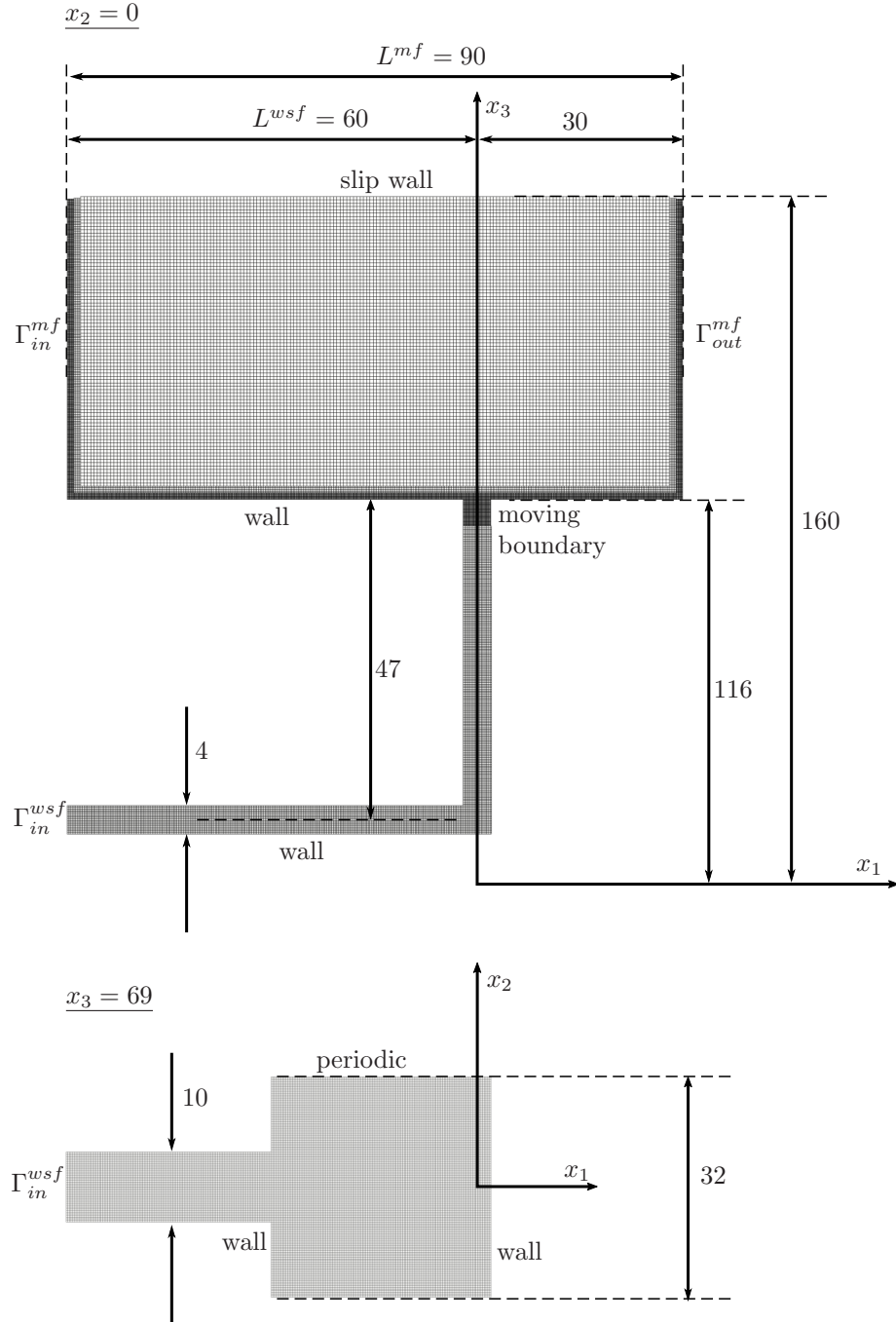
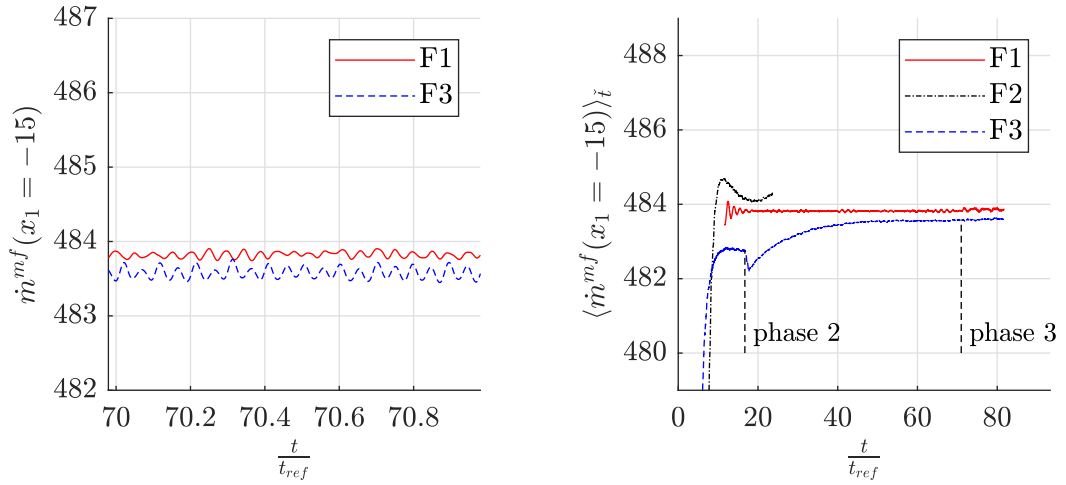


Figure 5.1: Computational domain of the turbine-like test case.

5.1 Main Flow

First, the main flow above $x_3 > 116$ is evaluated. In Fig. 5.2a, the instantaneous mass flow rate \dot{m}^{mf} through a plane of the main annulus at $x_1 = -15$ is shown for a period of time equal to the approximate traversal time from main annulus inflow to outflow. The mass flow rate, shown in Fig. 5.2b, is averaged over intervals of $\Delta t/t_{ref} = 0.2$, in order to flatten out the small scale fluctuation shown in Fig. 5.2a. In test case F1 the flow velocity is instantly established at the inflow. The pressure wave generated by the injected mass flow is reflected at the domain boundaries. In case of the CBC, the establishment of the velocity is driven due to the difference between inflow and outflow pressure. After the prescribed inflow total pressure and outflow static pressure are set by the CBC, it takes a long time until the flow converges to the final mass flow rate. After the second phase is initialized in test case F3, the reduction of the relaxation coefficients leads to a rise of the mass flow rate, increasing the time to convergence to the final mass flow rate. Test case F2 does not converge in the calculated time, and is canceled before the reduction of the relaxation coefficients due to problems of the adjustment of the wheel space mass flow rate.



(a) Phase 2 (without turbulence).

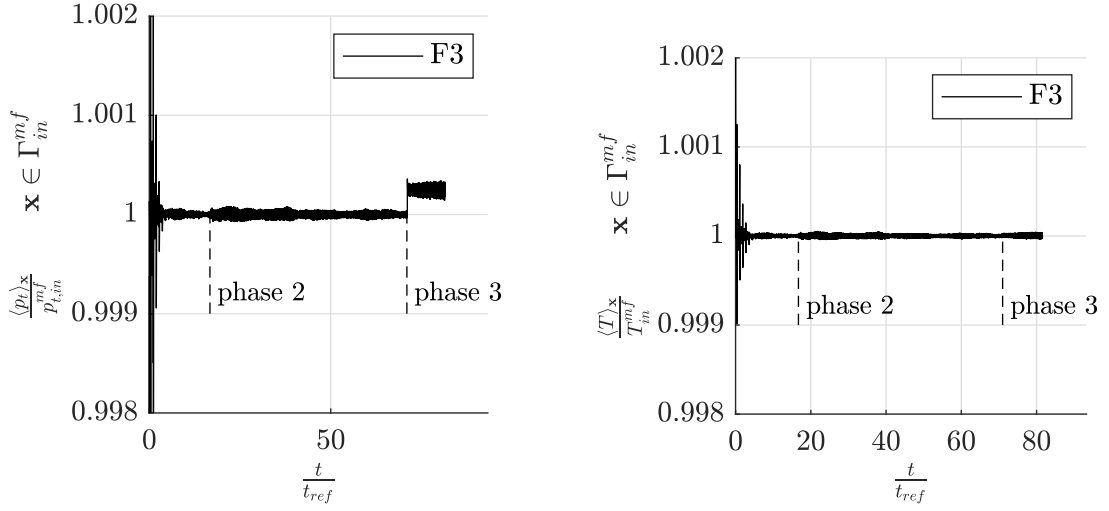
(b) Average in time,

$$\bar{t} \in \{t - 0.1t_{ref} < \bar{t} < t + 0.1t_{ref}\}.$$

Figure 5.2: Mass flow rate through a plane of the main annulus at $x_1 = -15$.

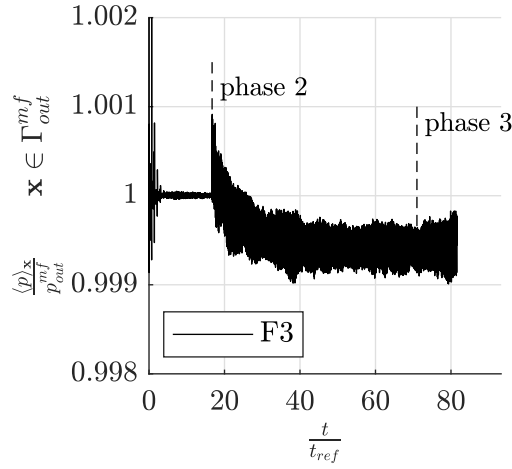
The regulated values at the inflow and outflow boundaries of the CBC in case F3 are presented in Fig. 5.3. Here, the values are averaged over the corresponding boundaries and normalized with the prescribed values. For high values of η_k and σ^* , the boundary conditions manage to keep the prescribed flow states. After the relaxation coefficients are lowered in the second phase, the static pressure at the outflow boundary drops leading to the rise of the mass flow rate through the main annulus as shown in Fig. 5.2b. The total pressure and static temperature of the characteristic main inflow condition are barely affected by the lowered

relaxation coefficients as shown in Fig. 5.3a and 5.3b. The turbulence injection in the third phase leads to a shift of the total pressure as shown in Fig. 5.3a.



(a) Total pressure $\langle p_t \rangle_{\mathbf{x}}$ averaged over the cells of the main annulus inflow Γ_{in}^{mf} and normalized with the target total pressure $p_{t,in}^{mf}$.

(b) Static temperature $\langle T \rangle_{\mathbf{x}}$ averaged over the cells of the main annulus inflow Γ_{in}^{mf} and normalized with the target static temperature T_{in}^{mf} .



(c) Static pressure $\langle p \rangle_{\mathbf{x}}$, averaged over the cells of the main annulus outflow Γ_{out}^{mf} and normalized with the target static pressure p_{out}^{mf} .

Figure 5.3: Imposed values at the main annulus inflow and outflow of test case F3.

5.2 Turbulence Injection into the Main Flow

For time $t/t_{ref} > 71.1$, synthetic turbulence generated by Eq. (3.68) is injected into the main annulus inflow of case F3. For comparison the same turbulence generated by Eq. (3.67) is imposed on the main annulus inflow of case F1 at $t/t_{ref} > 71.25$. The injected turbulence is evaluated using the temporally and spatially averaged Reynolds stresses $\langle \langle u'_i u'_i \rangle_t \rangle_{x_2, x_3}$ and turbulent kinetic energy $\langle \langle TKE \rangle_t \rangle_{x_2, x_3}$. In Fig. 5.4, the values are averaged at the end of the third phase over an interval of $\Delta t/t_{ref} = 2.09$.

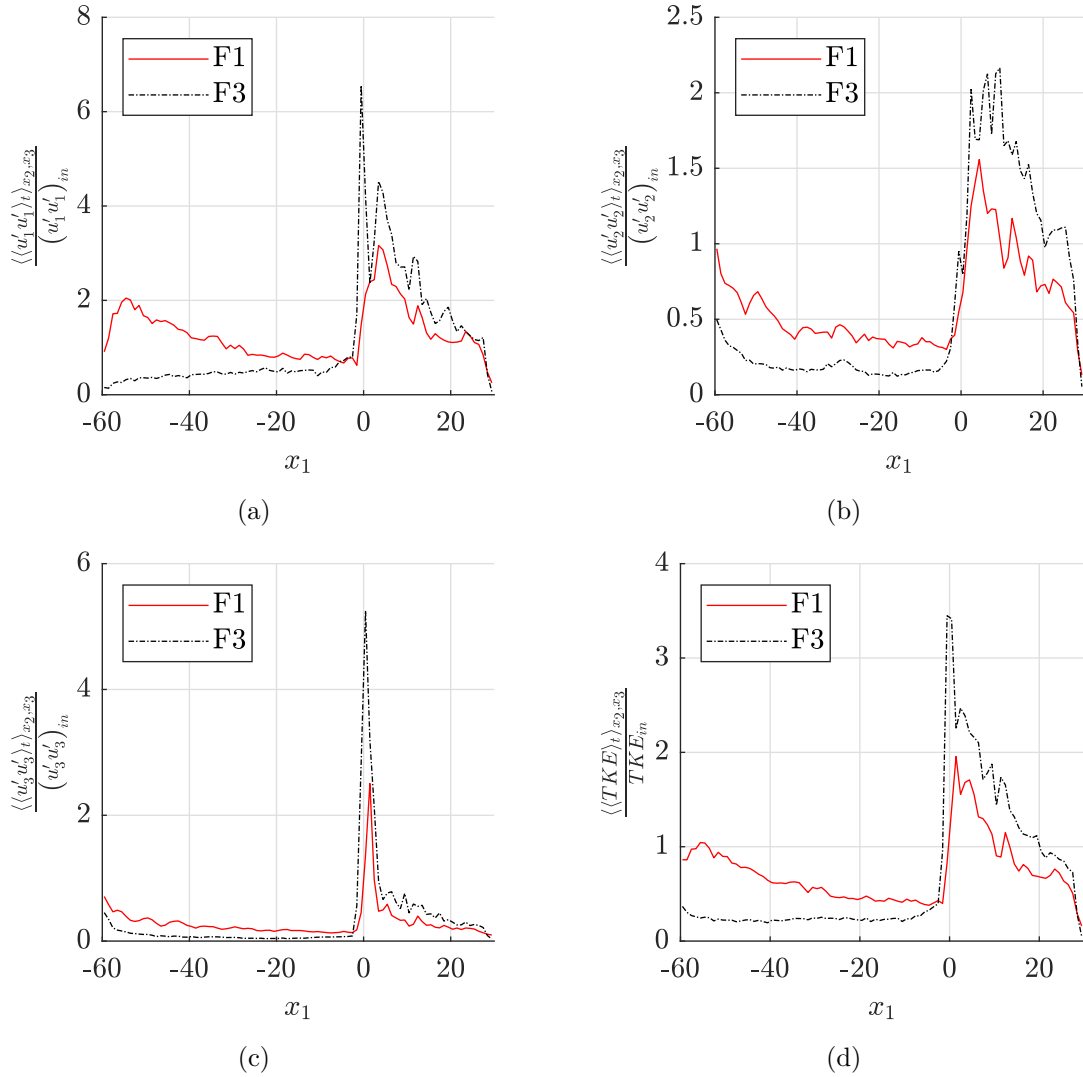


Figure 5.4: Reynolds stresses $\langle \langle u'_i u'_i \rangle_t \rangle_{x_2, x_3}$ and the turbulent kinetic energy $\langle \langle TKE \rangle_t \rangle_{x_2, x_3}$ spatially averaged over the x_2 - x_3 -planes of the main annulus, temporally averaged and normalized with the injected mean values $(\rho u'_i u'_i)_{in}$ and $(TKE)_{in}$.

The relaxation coefficients η_k of the turbine-like test case are chosen higher compared to the test case found in section 4.2 in order to achieve a stable solution. This leads to a significant

damping effect on the Reynolds stresses and the turbulent kinetic energy. The effect of high relaxation coefficients damping the injected turbulence is also described by Odier et al. [13]. Similar as in section 4.2, the Reynolds stress in flow direction is even lower than the tangential Reynolds stresses. At the position $x_1 = -2$, the influence of the wheel space and the imposed wall velocity on the turbulence can be observed.

5.3 Wheel Space Flow

For the test case F3, velocity and static temperature are imposed at the wheel space inflow using the CBC in Eq. 3.48. The imposed velocity in x_1 -direction is shown in Fig. 5.5a, spatially averaged over the inflow boundary and normalized by the target velocity. The prescribed temperature of the wheel space inflow can be observed in Fig. 5.5b also averaged over the boundary and normalized with the target temperature.

The velocity oscillates around a value of $u_1/u_{1,in}^{wsf} = 0.8256$ near the target velocity, while the amplitude is up to 15 times higher compared to the target $u_{1,in}^{wsf}$. The averaged static temperature converges slightly below the imposed values. The amplitudes of the temperature oscillations are relatively small compared to the velocity oscillations.

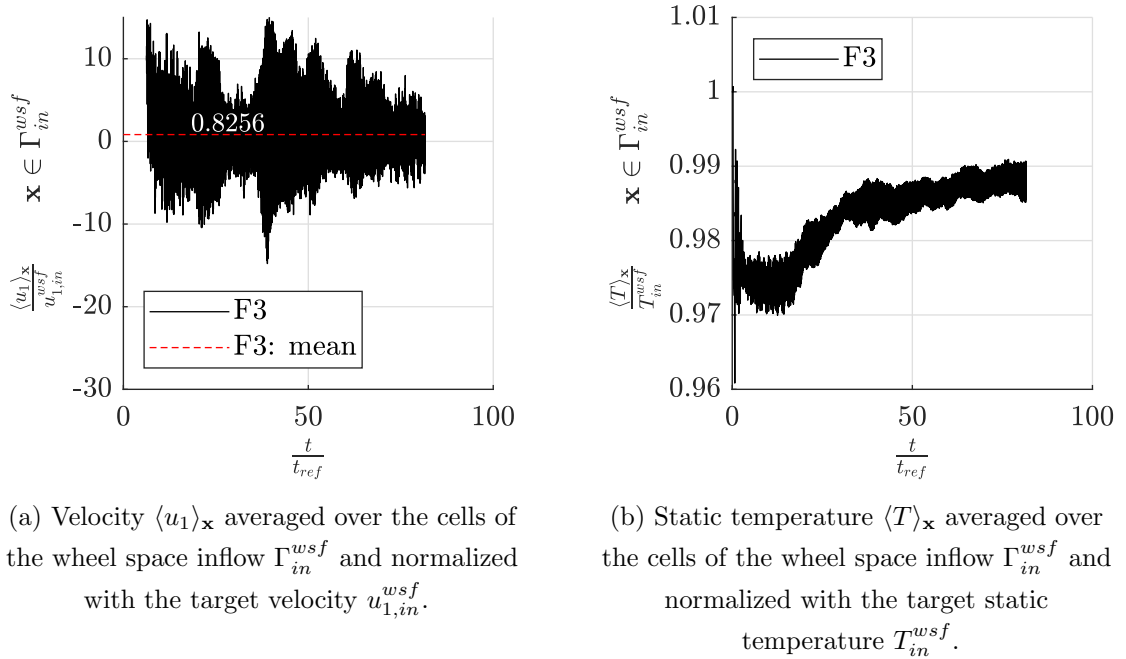
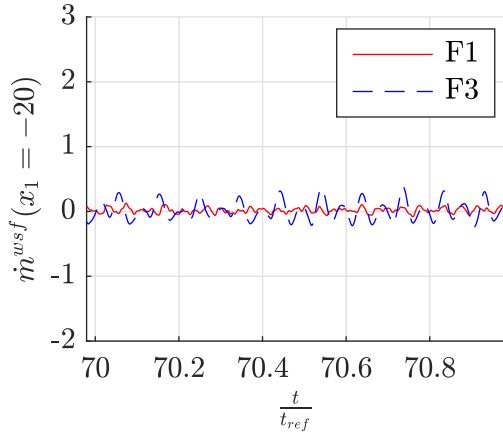


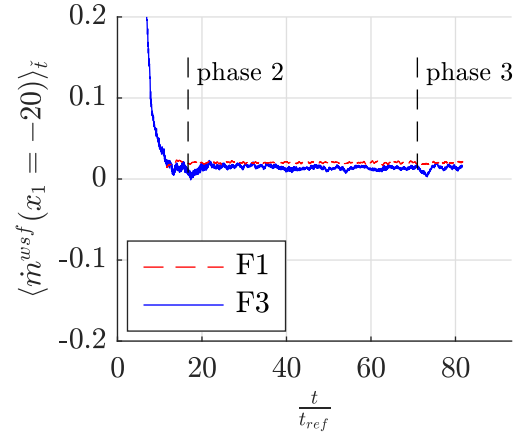
Figure 5.5: Imposed values at the wheel space inflow of the test case F3.

The mass flow rates through two planes in the wheel space located at $x_1 = 20$ and $x_3 = 90$ are shown in Fig 5.6. Here, the second plane is closer to the main flow. A positive mass flow rate indicates egress of the wheel space flow into the main flow. In Fig. 5.6a and 5.6c, the instantaneous mass flow rate is shown in absence of turbulence injection. The mass flow rates

of both test cases inside the wheel space are fluctuating about mean mass flow rates. These mean values are calculated between phase 2 and phase 3. For test case F3 the temporally averaged mass flow rate is $\dot{m} = 0.0139$ near the wheel space inflow at $x_1 = -20$ and $\dot{m} = 0.0127$ at $x_3 = 90$. For test case F1, the averaged mass flow rate is $\dot{m} = 0.0142$ at $x_1 = -20$ and $\dot{m} = -0.067$ at $x_3 = 90$. The fluctuations are multiple factors higher compared to the mean values. Fig. 5.6b and 5.6d show the time averaged mass flow rates averaged over intervals of $\Delta t/t_{ref} = 1.62$ in order to visualize the mean flow directions.

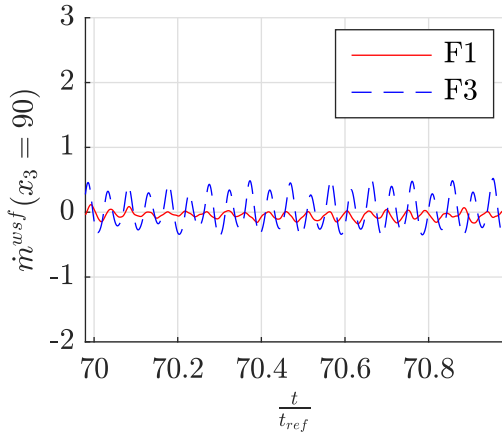


(a) Phase 2 (without turbulence).

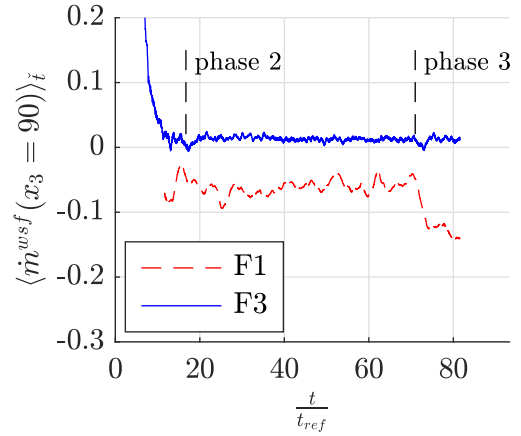


(b) Average in time,

$$\tilde{t} \in \{t - 0.81t_{ref} < \tilde{t} < t + 0.81t_{ref}\}.$$



(c) Phase 2 (without turbulence).



(d) Average in time,

$$\tilde{t} \in \{t - 0.81t_{ref} < \tilde{t} < t + 0.81t_{ref}\}.$$

Figure 5.6: Mass flow rates through the wheel space.

For case F1 in Fig. 5.6b, the mean mass flow rate through the plane near the wheel space inflow at $x_1 = -20$ remains positive, while in Fig. 5.6d the mass flow rate near the main annulus at $x_3 = 90$ remains negative. The density in the volume between the two planes increases due to the accumulation of mass. This implies that the calculation is not converged since a final density equilibrium is not reached. In Fig. 5.6b and 5.6d, the mass flow rate of

case F3 is positive through both planes, although the flow field of case F3 might also not be converged yet.

In the following, pressure, density and velocity fields are evaluated inside the wheel space. The instantaneous pressure field is shown for the test cases F1 and F3 in Fig. 5.7 at $t/t_{ref} \approx 71$. In Fig. 5.7, acoustic waves arise inside the wheel space and traverse into the main flow for both test cases, F1 and F3. Here, the pressure waves of test case F3 reach higher amplitudes. For test case F1, additional acoustic waves are moving along the periodic boundary condition in positive x_2 -direction as shown in Fig. 5.7c between $-30 < x_1 < -10$. Similar acoustic waves, moving along the periodic boundary, are not present in the test case F3.

The instantaneous density field is shown in Fig. 5.8 at $t/t_{ref} \approx 71$. A high density occurs near the edge at $x_1 = 2$ for case F1. This may be related to the accumulation of mass due to the mass flow rate from main annulus to the wheel space as shown in Fig. 5.6d. For the CBC in case F3, the instantaneous density field has a similar structure like the instantaneous pressure field. This is also the case for test case F1 in the area $-30 < x_1 < -10$.

The time averaged velocity fields of u_2 and u_3 are shown in Fig. 5.9 and 5.10. The velocity fields are averaged at the end of phase 2 before turbulence is injected over an interval of $\Delta t/t_{ref} = 6.3$. The velocity u_2 is largely influenced by the imposed wall velocity. The velocity distribution in both cases, F1 and F3, show large differences in the averaged u_2 -fields. In case F1, a higher velocity can be observed at the lower regions for $x_3 < 95$. This development may be connected to the negative mass flow rate shown in Fig. 5.6d. The injected mass is not transported out of the wheel space, accumulates and is accelerated by the imposed wall velocity. The averaged u_3 -field is shown in Fig. 5.10. For case F3, higher positive values can be observed inside the wheel space cavity. Further, the ingress from main annulus into wheel space does not reach as far into the wheel space compared to test case F1.

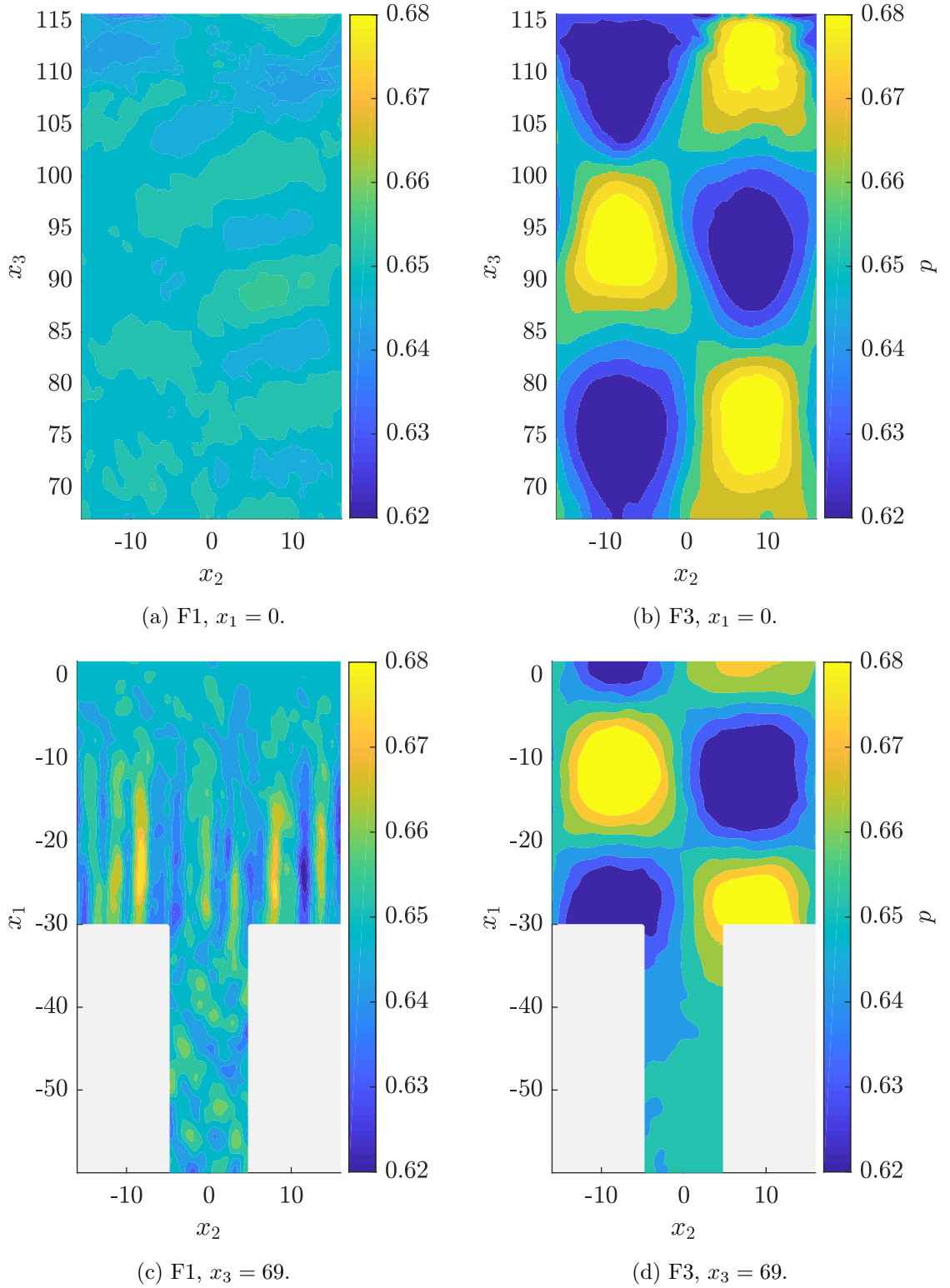


Figure 5.7: Instantaneous pressure fields in the wheel space at $t/t_{ref} \approx 71$ and without turbulence injection.

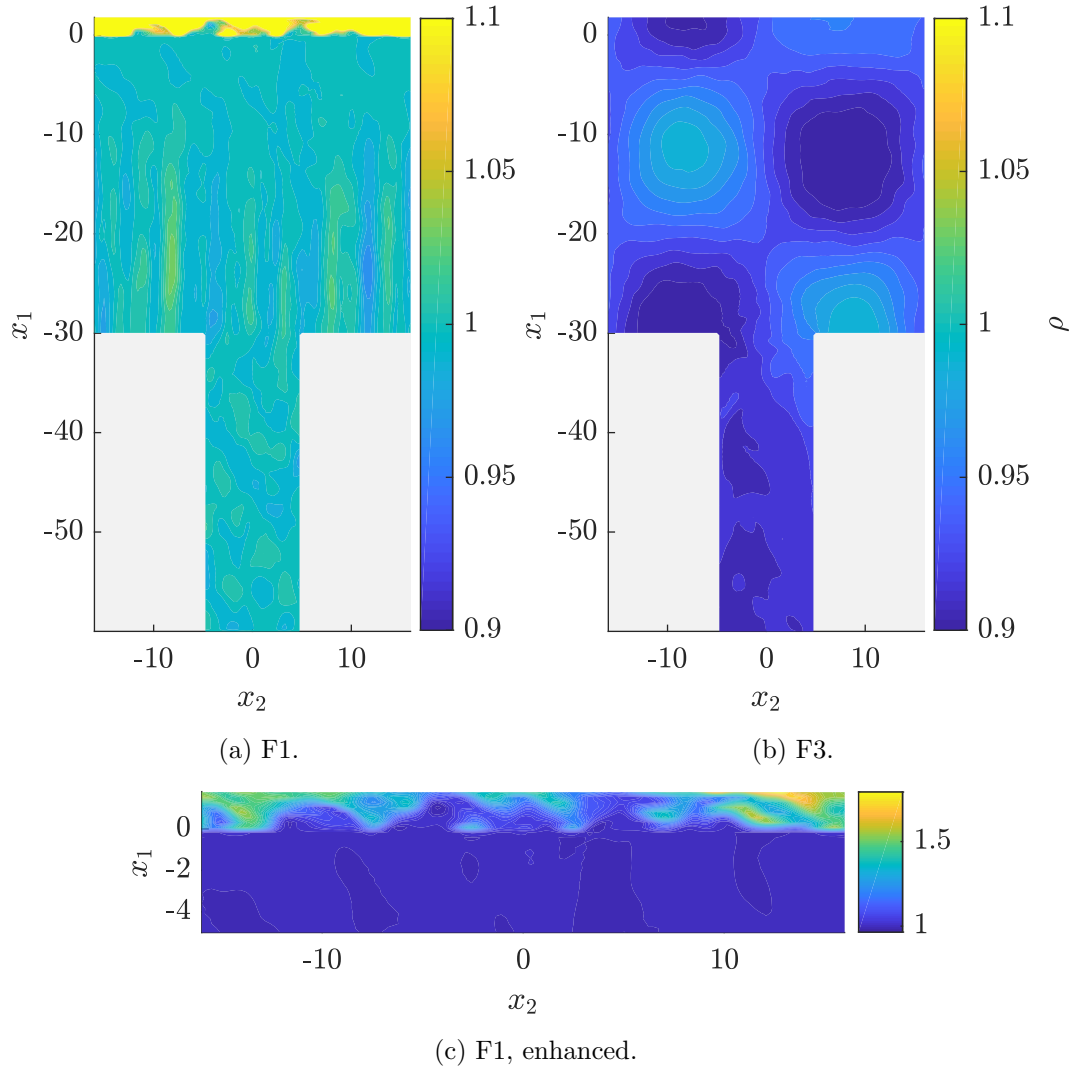


Figure 5.8: Instantaneous density fields in the wheel space at $x_3 = 69$, $t/t_{ref} \approx 71$ and without turbulence injection.

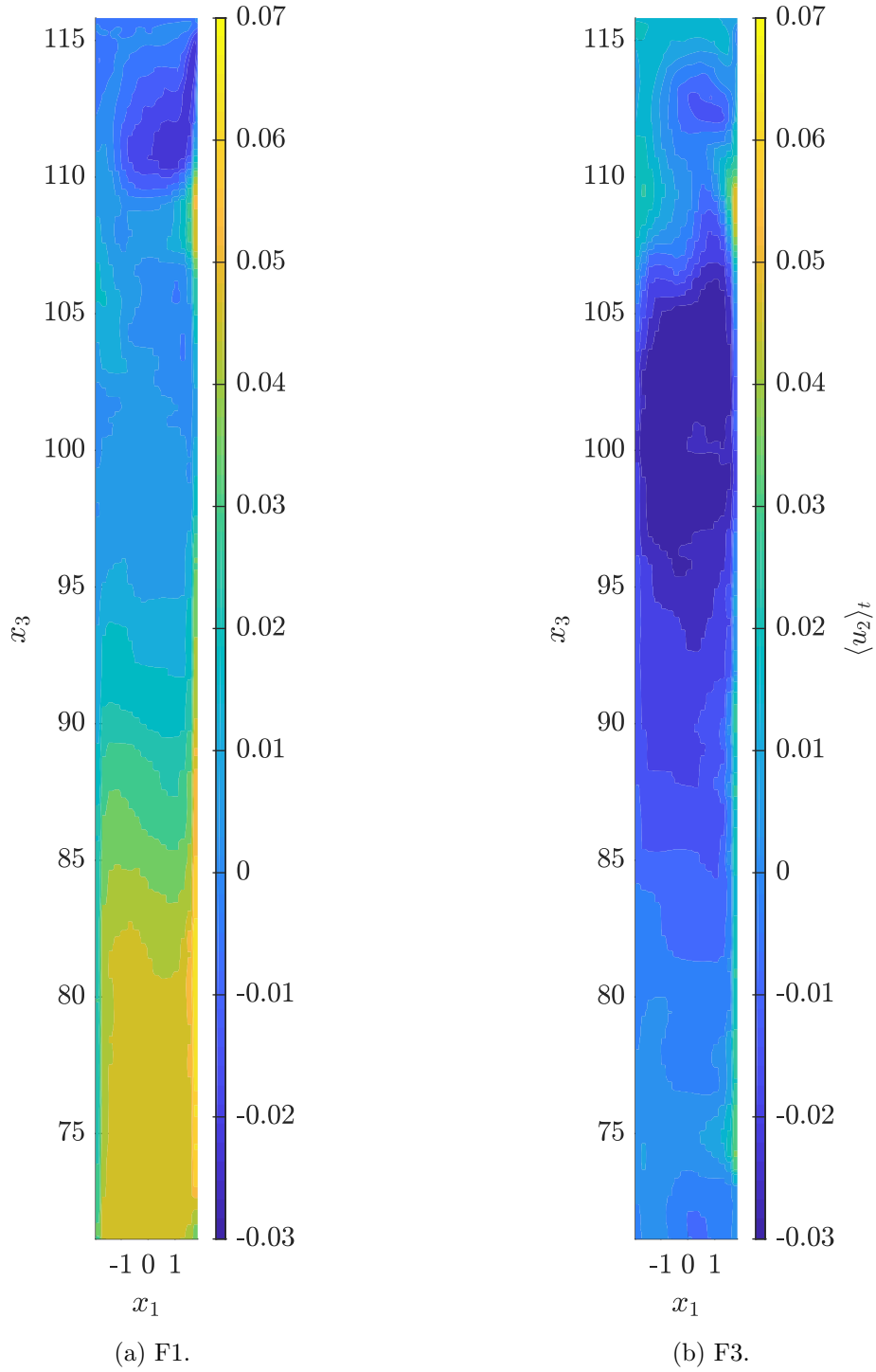
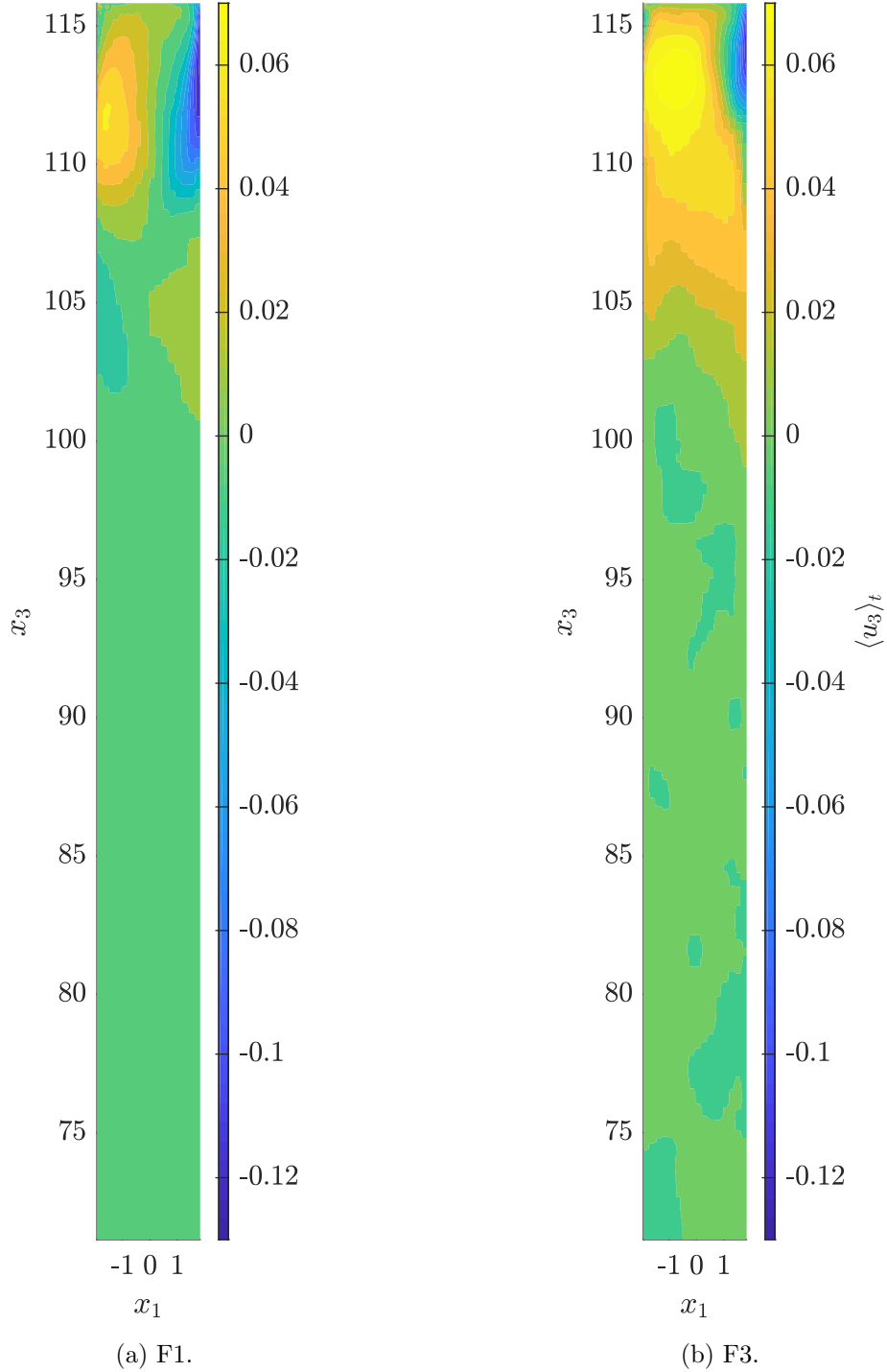


Figure 5.9: Time averaged velocity fields $\langle u_2 \rangle_t$ in the wheel space at $x_2 = 0$.

Figure 5.10: Time averaged velocity fields $\langle u_3 \rangle_t$ in the wheel space at $x_2 = 0$.

5.4 Evaluation of the Spectral Sound Pressure Level

The acoustic waves, arising inside the wheel space and spreading to the inflow and outflow boundaries of the domain, are evaluated using the spectral sound pressure level SPL. The SPL is calculated as

$$SPL = 10 \log \left(\frac{p_s'^2}{p_{ref}^2} \right) \quad (5.1)$$

with a reference pressure of $p_{ref} = \frac{2 \cdot 10^{-5} \text{ Pa}}{1.225 \text{ kg/m}^3 \cdot (340.21 \text{ m/s})^2} = 1.4106 \cdot 10^{-10}$. The reference pressure is the threshold of human hearing. This value is non-dimensionalized using standard density and speed of sound at a temperature of approximately 15°C . The spectral pressure fluctuations p_s are calculated using Welch's power spectrum density estimation. The SPL is plotted in a logarithmic scale along the Strouhal number,

$$Str = L_x^{mf} \cdot f / u_{in}^{mf}, \quad (5.2)$$

with the frequency f . It is $h = 3333$ the size of the Hamming window, $ol = 0$ the overlap and $n_s = 200\,000$ the number of samples recorded with a sampling frequency of $f_s \cdot t_{ref} = 4.78 \cdot 10^3$. The SPL are evaluated at inflow and outflow CBC of test case F3. The pressure fluctuations, used in Welch's power spectrum density estimation, are averaged over the cells of the corresponding boundary. Further, a plane inside the wheel space at $x_3 = 90$ is evaluated for the test cases F1 and F3. Here, the pressure is averaged over the cells of the planes. The pressure data used to calculate the spectrum is recorded without turbulence injection. The SPL are shown in Fig. 5.11.

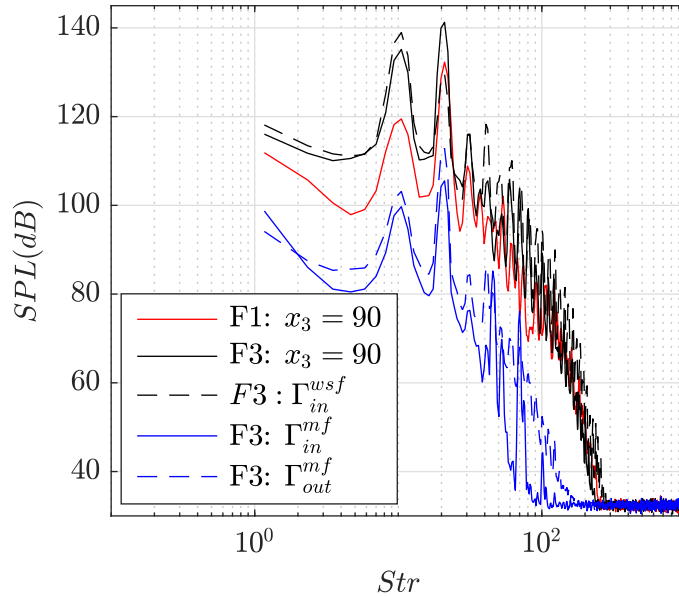


Figure 5.11: Spectral sound pressure level for various planes of the test cases F1 and F3.

It is notable that the energetic relevant power densities, including the spectrum inside the wheel space of case F1, peak at the same Strouhal numbers, namely $Str_1 = 10.5$ and $Str_2 = 21.01$. From the Strouhal numbers, a corresponding wavelength of the acoustic waves can be approximated using the equation

$$\omega = \frac{\langle a \rangle_{\mathbf{x}} L_x^{mf}}{Str u_{in}^{mf}} = \frac{\langle a \rangle_{\mathbf{x}} t_{ref}}{Str}, \quad \mathbf{x} \in \Gamma^{wsf}. \quad (5.3)$$

The speed of sound a is averaged over the wheel space domain as $\langle a \rangle_{\mathbf{x}} = 0.9617$. This leads to the wavelengths $\omega_1 = 22.58$ and $\omega_2 = 11.29$. The wavelengths ω_2 and ω_3 may relate to the pressure waves shown in Fig. 5.7, but this cannot be proven with the collected pressure data. Information about the frequencies is lost due to the spatial averaging. Regardless, the results in Fig. 5.11 are shown to give some insight into the similarities between test cases F1 and F3. Interesting for future work is the influence of the relaxation coefficients η_k , η_k^* and σ on the fluctuation and the frequency spectrum. Here, the inflow of the wheel space is of special interest due to the high amplitudes of the fluctuations, but this goes beyond the scope of this work.

Chapter 6

Conclusion

Within the scope of this work, a partially non-reflecting Characteristic Boundary Condition (CBC) has been derived, based on the work of Odier et al. [13], imposing total pressure, static temperature and tangential velocities. The derived boundary condition has been implemented into the framework of ZFS. Additional partially non-reflecting CBC have been implemented including an inflow condition, imposing velocity and static temperature, as well as an outflow condition, imposing mean static pressure. Furthermore, a method to inject a synthetic turbulence field into a CBC was implemented. The implementations of the numerical methods have been evaluated in multiple test cases with the main focus on the alignment of the prescribed values and the partial non-reflectivity. Finally, the boundary conditions were applied to a turbine-like setup and compared to a calculation using Neumann and Dirichlet type boundary conditions.

All implemented CBC managed to reach and adhere the prescribed values in the test cases found in chapter 4. Further, it has been shown that the implemented inflow CBC, imposing total pressure, static temperature and tangential velocities, as well as the outflow CBC, imposing mean static pressure, hold the property of partial non-reflectivity. The method to inject synthetic turbulence via CBC was not able to reproduce the desired turbulence. While the turbulence in tangential directions reached the target values of the injected turbulence field, the turbulence intensity in flow direction was multiple factors lower as the target values. The outflow CBC, imposing mean static pressure, managed to represent a rotational flow, as well as vortices leaving the computational domain.

The application of the CBC in the turbine-like setup in chapter 5 showed great differences between CBC and Neumann and Dirichlet type boundary condition inside the turbine wheel space. While the test case using the CBC showed a flow from wheel space into the main flow, the Neumann and Dirichlet type boundary conditions led to an ingress from main annulus into the wheel space and an accumulation of mass inside the wheel space. The difference in

the rate of convergence to a final state between both test cases is not clear since the test cases did not converge in the expected time. It is noticeable, that the CBC at the main stage inflow showed a necessity for higher relaxation coefficients compared to the less complex test cases injecting turbulence in section 4.2. Nonetheless, the CBC remains partially non-reflective, but the high relaxation coefficients prevent the injection of turbulence. The CBC at the wheel space inflow showed large fluctuations around the imposed velocity. Since the relaxation coefficients have a large impact on those fluctuations, the question comes up, how the optimal relaxation coefficients for the complex flow conditions at the inflow of a turbine wheel space can be found.

Building on the work of this thesis, the turbulence injection may be further investigated. Part of this investigation is the influence of the turbulence injection on the Reynolds stress in flow direction. Further, the question arises if the damping of the turbulence with high relaxation coefficients can be prevented. Another important topic for future works is the adjustment of the inflow relaxation coefficients at the wheel space inflow boundary. High velocity fluctuations could be observed at the wheel space inflow CBC. The influence of the relaxation coefficients on the amplitude and on the spectral distribution of these fluctuations may be part of further investigations.

Bibliography

- [1] P. Batten, U. Goldberg, and S. Chakravarthy. Interfacing statistical turbulence closures with large-eddy simulation. *AIAA J.*, 42(3):485–492, 2004. doi:10.2514/1.3496.
- [2] M. Berger, M. J. Aftosmis, and S. R. Allmaras. Progress towards a cartesian cut-cell method for viscous compressible flow. *AIAA Paper 2012-1301*, 2012. doi:10.2514/6.2012-1301.
- [3] J. P. Boris, F. F. Grinstein, E. S. Oran, and R. L. Kolbe. New insights into large eddy simulation. *Fluid Dyn. Res.*, 10(4–6):199–228, 1992. doi:10.1016/0169-5983(92)90023-P.
- [4] B. Engquist and A. Majda. Absorbing boundary conditions for numerical simulation of waves. *Proc. Natl. Acad. Sci. U.S.A.*, 74(5):1765–1766, 1977. doi:10.1073/pnas.74.5.1765.
- [5] J. B. Freund. Proposed inflow/outflow boundary condition for direct computation of aerodynamic sound. *AIAA J.*, 35(4):740–742, 1997. doi:10.2514/2.167.
- [6] F. Gao, J. W. Chew, P. F. Beard, D. Amirante, and N. J. Hills. Large-eddy simulation of unsteady turbine rim sealing flows. *Int. J. Heat Fluid Flow*, 70:160–170, 2018. doi:10.1016/j.ijheatfluidflow.2018.02.002.
- [7] V. Granet, O. Vermorel, T. Léonard, L. Gicquel, and T. Poinso. Comparison of nonreflecting outlet boundary conditions for compressible solvers on unstructured grids. *AIAA J.*, 48(10):2348–2364, 2010. doi:10.2514/1.J050391.
- [8] N. Guézennec and T. Poinso. Acoustically nonreflecting and reflecting boundary conditions for vorticity injection in compressible solvers. *AIAA J.*, 47(7):1709–1722, 2009. doi:10.2514/1.41749.
- [9] C. Koupper, T. Poinso, L. Gicquel, and F. Duchaine. Compatibility of characteristic boundary conditions with radial equilibrium in turbomachinery simulations. *AIAA J.*, 52(12):2829–2839, 2014. doi:10.2514/1.J052915.

- [10] A. Lintermann, S. Schlimpert, J. H. Grimmer, C. Günther, M. Meinke, and W. Schröder. Massively parallel grid generation on hpc systems. *Comput. Methods Appl. Mech. Eng.*, 277:131–153, 2014. doi:10.1016/j.cma.2014.04.009.
- [11] G. Lodato, P. Domingo, and L. Vervisch. Three-dimensional boundary conditions for direct and large-eddy simulation of compressible viscous flows. *J. Comput. Phys.*, 227(10):5105–5143, 2008. doi:10.1016/j.jcp.2008.01.038.
- [12] M. Meinke, W. Schröder, E. Krause, and T. Rister. A comparison of second- and sixth-order methods for large-eddy simulations. *Comput. Fluids*, 31(4–7):695–718, 2002. doi:10.1016/S0045-7930(01)00073-1.
- [13] N. Odier, M. Sanjosé, L. Gicquel, T. Poinso, S. Moreau, and F. Duchaine. A characteristic inlet boundary condition for compressible, turbulent, multispecies turbomachinery flows. *Comput. Fluids*, 178:41–55, 2019. doi:10.1016/j.compfluid.2018.09.014.
- [14] T. S. D. O’Mahoney, N. J. Hills, J. W. Chew, and T. Scanlon. Large-eddy simulation of rim seal ingestion. *Proc. Inst. Mech. Eng. C*, 225(12):2881–2891, 2011. doi:10.1177/0954406211409285.
- [15] A. Pogorelov, M. Meinke, and W. Schröder. Large-eddy simulation of the unsteady full 3d rim seal flow in a one-stage axial-flow turbine. *Flow Turbul. Combust.*, 102(1):189–220, 2019. doi:10.1007/s10494-018-9956-9.
- [16] T. J. Poinso and S. K. Lele. Boundary conditions for direct simulations of compressible viscous flows. *J. Comput. Phys.*, 101(1):104–129, 1992. doi:10.1016/0021-9991(92)90046-2.
- [17] R. Prosser. Improved boundary conditions for the direct numerical simulation of turbulent subsonic flows. i. inviscid flows. *J. Comput. Phys.*, 207(2):736–768, 2005. doi:10.1016/j.jcp.2005.01.027.
- [18] D. H. Rudy and J. C. Strikwerda. A nonreflecting outflow boundary condition for subsonic navier-stokes calculations. *J. Comput. Phys.*, 36(1):55–70, 1980. doi:10.1016/0021-9991(80)90174-6.
- [19] L. Schneiders, C. Günther, M. Meinke, and W. Schröder. An efficient conservative cut-cell method for rigid bodies interacting with viscous compressible flows. *J. Comput. Phys.*, 311:62–86, 2016. doi:10.1016/j.jcp.2016.01.026.
- [20] L. H. Smith Jr. The radial-equilibrium equation of turbomachinery. *J. Eng. Power*, 88(1):1–12, 1966. doi:10.1115/1.3678471.

-
- [21] J. C. Sutherland and C. A. Kennedy. Improved boundary conditions for viscous, reacting, compressible flows. *J. Comput. Phys.*, 191(2):502–524, 2003. doi:10.1016/S0021-9991(03)00328-0.
- [22] K. W. Thompson. Time dependent boundary conditions for hyperbolic systems. *J. Comput. Phys.*, 68(1):1–24, 1987. doi:10.1016/0021-9991(87)90041-6.
- [23] B. Thornber, A. Mosedale, D. Drikakis, D. Youngs, and R. J. R. Williams. An improved reconstruction method for compressible flows with low mach number features. *J. Comput. Phys.*, 227(10):4873–4894, 2008. doi:10.1016/j.jcp.2008.01.036.
- [24] C. S. Yoo and H. G. Im. Characteristic boundary conditions for simulations of compressible reacting flows with multi-dimensional, viscous and reaction effects. *Combust. Theory and Model.*, 11(2):259–286, 2007. doi:10.1080/13647830600898995.
- [25] C. S. Yoo, Y. Wang, A. Trouvé, and H. G. Im. Characteristic boundary conditions for direct simulations of turbulent counterflow flames. *Combust. Theory Model.*, 9(4):617–646, 2005. doi:10.1080/13647830500307378.